OLD DOMINION UNIVERSITY RESEARCH FOUNDATION

DEPARTMENT OF MECHANICAL ENGINEERING AND MECHANICS
SCHOOL OF ENGINEERING
OLD DOMINION UNIVERSITY
NORFOLK, VIRGINIA

EFFECTS OF PRECURSOR HEATING ON CHEMICAL AND RADIATIVE NONEQUILIBRIUM VISCOUS FLOW AROUND A JOVIAN ENTRY BODY

By

S. N. Tiwari

and

K. Y. Szema

Progress Report
For the period February 1, 1978 to July 31, 1978

Prepared for the
National Aeronautics and Space Administration
Langley Research Center
Hampton, Virginia

Under
Research Grant NSG 1492
Randolph A. Graves, Jr., Technical Monitor
Space Systems Division

December 1978

DEPARTMENT OF MECHANICAL ENGINEERING AND MECHANICS
SCHOOL OF ENGINEERING
OLD DOMINION UNIVERSITY
NORFOLK, VIRGINIA

EFFECTS OF PRECURSOR HEATING ON CHEMICAL AND RADIATIVE NONEQUILIBRIUM VISCOUS FLOW AROUND A JOVIAN ENTRY BODY

By

S. N. Tiwari

and

K. Y Szema

Progress Report
For the period February 1, 1978 to July 31, 1978

Prepared for the
National Aeronautics and Space Administration
Langley Research Center
Hampton, Virginia 23665

Under
Research Grant NSG 1492
Randolph A. Graves, Jr., Technical Monitor
Space Systems Division

Submitted by the
Old Dominion University Research Foundation
P. O. Box 6369
Norfolk, Virginia 23508

December 1978

FOREWORD

This report covers work completed during the period February 1, 1978 through July 31, 1978 on the research project "Influence of Precursor Heating on Nonequilibrium Viscous Flow Around a Jovian Entry Body." The work was supported by the NASA/Langley Research Center (Aerothermodynamics Branch of the Space Systems Division) through research grant NSG 1492. The grant was monitored by Dr. Randolph A. Graves, Jr. of SSD-Aerothermodynamics Branch (Mail Stop 366).

TABLE OF CONTENTS

LIST OF TABLES

LIST OF FIGURES

LIST OF FIGURES (CONCL'D)

EFFECTS OF PRECURSOR HEATING ON CHEMICAL AND RADIATIVE NONEQUILIBRIUM VISCOUS FLOW AROUND A JOVIAN ENTRY BODY

By

S. N. Tiwari[1] and K. Y. Szema[2]

SUMMARY

The influence of precursor heating on viscous chemical nonequilibrium radiating flow around a Jovian entry body is investigated. Results obtained for a 45-degree hyperboloid blunt body entering Jupiter's nominal atmosphere at zero angle of attack indicate that the nonequilibrium radiative heating rate is significantly higher than the corresponding equilibrium heating. The precursor heating, in general, increases the radiative and convective heating to the body, and this increase is slightly higher for the nonequilibrium conditions.

NOMENCLATURE

C_i	mass fraction of species i in the shock layer, ρ_i/ρ
J_i	mass diffusion flux of species i
k	Boltzmann constant
k_b,r	backward rate constant
k_c,r	equilibrium rate constant
k_f,r	forward rate constant
Le	Lewis number
M*	molecular weight of mixture
N	number of moles

[1] Professor, Department of Mechanical Engineering and Mechanics, Old Dominion University, Norfolk, Virginia 23508.

[2] Graduate Research Assistant, Old Dominion University Research Foundation, P. O. Box 6369, Norfolk, Virginia 23508.

n	coordinate normal to the bow shock, n^*/R_N^*
p	pressure, $p^*/(\rho_\infty^* V_\infty^{*2})$
Pr	Prandtl number, $\mu^* C_p^*/k^*$
q_R	net radiant heat flux, $q_R^*/(\rho_\infty^* V_\infty^{*3})$
r	radius measured from axis of symmetry to a point on the body surface, r^*/R_N^*
r_s	radius measured from axis of symmetry to a point on the bow shock, r_s^*/R_N^*
R^*	universal gas constant
R_b^*	radius of the body
R_N^*	body nose radius (same as R_n^*)
R_s^*	radius of the bow shock
s	coordinate along the bow shock, s^*/R_N^*
T	temperature, T^*/T_{ref}^*
T_{ref}^*	reference temperature, $V_\infty^*/C_{p\infty}^*$
u	velocity tangent to body surface, u^*/V_∞^*
u'	velocity tangent to bow shock, cm/sec
v	velocity normal to body surface, u^*/V_∞^*
v'	velocity normal to bow shock, cm/sec
x	coordinate along the body surface, x^*/R_N^*
y	coordinate normal to the body surface, v^*/R_N^*
α	shock angle defined in figure 1
ϵ	Reynolds number parameter or surface emittance
θ	body angle defined in figure 1
η	transformed y coordinate, y/v_s
κ	body curvature, $\kappa^* R_N^*$
μ	viscosity of mixture, μ^*/μ_{ref}^*
μ_{ref}^*	reference viscosity, $\mu^*(T_{ref}^*)$

ξ coordinate along the body surface, $\xi=x$

ρ density of mixture, ρ^*/ρ^*_∞

Subscript

i ith species

s shock value

w wall value

∞ free-stream condition

ν radiation frequency

1. INTRODUCTION

In two previous studies (refs. 1 and 2), the authors have investigated the influence of precursor heating on the flow phenomena around a Jovian entry body. In these studies, the precursor as well as shock-layer gas was assumed to be in chemical nonequilibrium. While for most entry conditions envisioned for Jupiter's atmosphere it may be reasonable to assume chemical equilibrium in the precursor region, this assumption could not be justified logically for the shock layer. This is because (aside from inclusion of the precursor effect) there exists strong evidence of a significantly large chemical nonequilibrium layer (closer to the shock) in the shock layer for Jovian entry conditions (refs. 3 to 6). Also, sutdies on heating of high-speed vehicles entering other planetary atmospheres (refs. 7 to 10) have indicated that, under certain conditions, the radiation from the nonequilibrium region of the shock layer was considerably higher than that predicted by an equilibrium analysis.

The purpose of this study, therefore, is to investigate the influence of precursor heating on the flow phenomena around a Jovian entry body under the chemical nonequilibrium in the shock layer. The reaction scheme (which includes hydrogen dissociation, electronic excitation, and ionization by atom-atom and atom-electron collisions) proposed by Leibowitz (ref. 3) is used in this study. Ionization of hydrogen is initiated by atom-atom collisions which produce atoms in electronically excited states. These are rapidly

ionized by additional collisions. A simplified two-step model is assumed in which hydrogen in the first excited state is produced by collisions with hydrogen and helium atoms and is then immediately ionized by a subsequent collision. The hydrogen is then ionized by collisions with electrons. Molecular hydrogen is first dissociated by collisions with itself and helium. The hydrogen atoms produced in the reaction also participate in the dissociation reaction as do ions and electrons as they are formed. The solutions of the governing viscous shock layer and inviscid precursor equations are obtained by employing the numerical procedures outlined in references 1 and 2.

2. ANALYSIS

The physical model and coordinate system for a Jovian entry body is shown in figure 1. As discussed in references 1 and 2, the entire flow field ahead of the body is divided into three regions: the free stream, the precursor region (preheating zone), and the shock layer. The basic governing equations and boundary conditions for the present problem are essentially the same as those given in reference 2. There are, however, a few definite changes in the governing equations because of the chemical nonequilibrium condition, and these are discussed briefly in this section.

2.1. Governing Equations for the Precursor Region

The precursor region is considered to be thin, and the flow in this region is assumed to be steady, inviscid, and in chemical equilibrium. The governing equations for this region, therefore, are the same as those given in reference 2. Because of the chemical nonequilibrium in the shock layer, however, the conditions at the outer edge of the shock are found to be different from those obtained in reference 2. It should be pointed out here that, for the coupled precursor-shock layer flow phenomena, the conditions at the outer edge of the shock are obtained through iterative procedures.

2.2. Shock-Layer Equations

The flow in the shock layer is assumed to be axisymmetric, steady, laminar, viscous and compressible. The shock layer gas is assumed to be in local thermodynamic equilibrium but in chemical nonequilibrium. The basic

governing equations (continuity, x-momentum, y-momentum, and energy), therefore, are the same ones given in reference 2. The species continuity equation, however, is different, and this is given by the relation

$$\rho\left[(u/\Gamma)(\partial C_i/\partial x) + v(\partial C_i/\partial y)\right] = \dot{w}_i \cdot (\epsilon^2/\Gamma\zeta) \cdot \left[(\partial/\partial y)\ (\Gamma\zeta J_i)\right] \tag{1}$$

where

$$\Gamma = 1 + y\kappa,\ \zeta = r + y\cos\theta,\ \epsilon = u^*_{ref}/(\rho^*_\infty V^*_\infty R^*_n)^{1/2},$$

$$J_i = (u/Pr)Le(\partial C_i/\partial y)$$

and $\dot{w}_i$ represents the rate of production of chemical species in the shock layer. The equation of state proposed by Zoby et al. (ref. 11) is valid only for chemical equilibrium conditions. In the case of chemical nonequilibrium, the equation of state is given by the relation (ref. 12)

$$p^*v^* = (\sum_i N_i)R^*T^* \tag{2}$$

where N_i is the number of moles for the ith species. This result is reminiscent of the thermal equation of state for a perfect gas. The sum in the parentheses, however, is not a constant since the total number of moles changes as the chemical balance changes. Other shock-layer equations are the same as those presented in reference 2.

As in reference 2, no-slip and no temperature-jump conditions are used at the body surface (wall). Thus, $u_w = v_w = 0$, and the wall temperature is either specified or calculated. Furthermore, it is assumed that the chemical species are in equilibrium at the body surface. The conditions in front of the shock are obtained from the precursor solutions; the conditions immediately behind the shock are obtained by using the Rankine-Hugoniot relations. Two assumptions can be made about the molecular hydrogen entering the shock layer immediately behind the shock. One criterion is to assume that chemical reactions are "completely frozen" and that initial composition of hydrogen just behind the shock corresponds to the free-stream value. The second

criterion is to consider that all hydrogen moledules have been dissociated immediately behind the shock. This is referred to as the "half frozen" condition. Both conditions are used in this study.

2.3. Rate of Species Production in the Shock Layer

The reaction scheme describing important collisional processes in hydrogen-helium ionizing shock waves has been modeled by Leibowitz (refs. 3 and 6) after the results of argon ionization studies. Eleven separate reaction steps describe the dissociation of molecular hydrogen, excitation of electronic states of hydrogen and helium, and ionization of the atomic hydrogen and helium by collisions with atoms and electrons. A complete discussion on these reaction schemes is available in reference 3, and a brief discussion is presented here. The eleven reactions and corresponding rate constants are given in table 1.

In a complex gas mixture containing a total of ℓ species of x_i, capable of undergoing m elementary chemical reactions, the chemical equation for the general elementary reaction r can be written as (ref. 12)

$$\sum_{i=1}^{\ell} a_{i,r}\, x_i \underset{k_{b,r}}{\overset{k_{f,r}}{\rightleftharpoons}} \sum_{i=1}^{\ell} b_{i,r}\, X_i \tag{3}$$

where $a_{i,r}$ and $b_{i,r}$ are the stochiometric coefficients appearing on the left and right in the reaction r. By applying the principle of detailed balancing, the backward rate constant, $k_{b,r}$, is obtained by dividing the forward rate constant, $k_{f,r}$, by the equilibrium constant $k_{c,r}$. The equilibrium constants for hydrogen, helium species were obtained by Leibowitz (ref. 3) by using the thermochemistry program of Horton and Menard (ref. 13). These constants were obtained also in a separate study by Zoby et al. (ref. 14) and are expressed here as

$$k_{H^+} = 4.05 \times 10^{-9}\, T^{3/2} \exp(-1.578 \times 10^5/T) \tag{4a}$$

$$k_{He^+} = 1.62 \times 10^{-8}\, T^{3/2} \exp(-2.853 \times 10^5/T) \tag{4b}$$

$$k_H = 3.7[1 - \exp(-1.5 \times 10^8/T^2)] \exp(-52340/T) \tag{4c}$$

The total rate of change in x_i is given by the relation (ref. 12)

$$\frac{dx_i}{dt} = \sum_{r=1}^{m} (b_{i,r}-a_{i,r})k_{f,r}\left[\prod_{i=1}^{\ell} (x_i)^{a_{i,r}} - \frac{1}{k_{c,r}} \prod_{i=1}^{\ell} (x_i)^{b_{i,r}}\right] \qquad (5)$$

This is the general rate equation for a complex gas mixture. The rate of production of chemical species, $\dot{w}_i$, now can be expressed by

$$\dot{w}_i = M_i^* \, (dx_i^*/dt) \, (R_n^*/\rho_\infty^* \, v_\infty^*) \qquad (6)$$

Equations (1) to (6), along with other fluid mechanical equations and the electron energy equation, are solved numerically to obtain the concentration of all species. In order to have a reasonable rate of convergence in the numerical scheme, however, it is important to express the rate of production term in a proper form. This is accomplished by splitting $\dot{w}_i$ into two separate contributions as (refs. 15-18)

$$\dot{w}_i/\rho = (\dot{w}_i)^0 - (\dot{w}_i)^1 \, C_i \qquad (7)$$

The reasons for doing this are explained in the cited references.

2.4. Electron Temperature

Because of a large ratio of atom (or ion) mass to electron mass, electrons transfer energy rapidly by collisions with other electrons but only slowly by elastic collisions with atoms or ions. Consequently, a different temperature is given to atoms (heavy particles) and electrons in the same gas. The electron temperature is obtained from the solution of the electron energy equation. A detailed discussion of the electron energy equation is given by Appleton and Bray (ref. 19). For a one-dimensional, steady shock wave in a H_2-He mixture, the resulting equation can be expressed as (ref. 3):

$$3[e]m_e \, \bar{\upsilon} R(T - Te) - \theta_H(R_1 - R_{1r} + R_3 - R_{3r}) - \theta_{He}(R_2 - R_{2r} + R_4 - R_{4r}) = 0 \qquad (8)$$

where

$$\nu_{ek} = n_k \, V_e \, Q_{ek} \tag{9a}$$

$$V_e = (8k \, Te/\Pi m_e)^{1/2} \tag{9b}$$

$$Q_{ek} = A_k[\exp(-a_k E) - \exp(-b_k E)] \tag{9c}$$

$$E = (1/2)V^2 \tag{9d}$$

$$V = 4(k \, Te/2\Pi\mu)^{1/2} \tag{9e}$$

$$\mu = m_a \, m_b/(m_a + m_b) \tag{9f}$$

$$\bar{\nu} = \sum_k \nu_{ek}/m_k \tag{9g}$$

In equation (8), [e] represents the concentration of electrons, θ_k is the ionization energy per mole of species k, and R_i and R_{ir} are the forward and backward production rates for electrons respectively. In equation (9a), ν_{ek} represents the collisional frequency, n_k is the number density of species k, V_e is the average electron velocity, and Q_{ek} represents the elastic collision cross section for species k. In equations (9d) and (9e), E represents the relative kinetic energy, V is the relative speed, and μ is the reduced mass. The values of coefficients A_k, a_k, and b_k appearing in equation (9c) are available in reference 3. By substituting equations (4a) to (4c) and (9a) to (9g) into equation (8), an implicit expression for the electron temperature, in terms of the species concentration and heavy particle temperature, can be obtained as

$$Te = T - [(k_1 + k_3)(x_2 - x_4/K_{C,H}) + (k_2 + k_4)(x_3 - x_5/K_{C,He})]/x_1 \tag{10}$$

where k_1, k_2, k_3, k_4 are rate constants in table 1 and

$$x_1 = 1/(3[e]m_e \, \bar{\nu} \, R) \tag{11a}$$

$$x_2 = \theta_H[H][e] \tag{11b}$$

$$x_3 = \theta_{He}[He][e] \tag{11c}$$

$$x_4 = \theta_{H}[H^+][e] \tag{11d}$$

$$x_5 = \theta_{He}[He^+][e] \tag{11e}$$

Use of the electron temperature is made in evaluating the radiative flux in the shock layer.

2.5. Radiation Transport Model

The radiation models used in this study are discussed in detail in references 1, 2, and 14. The radiative flux, q_R, is calculated with the assumption of nonscattering medium, the tangent slab approximation for radiative transfer, and nonreflecting bounding surfaces. The spectral absorption model for the hydrogen species in the precursor region is a three-step model and is described in reference 1. In the shock layer, the absorption by the helium species is usually neglected for most Jovian entry conditions. In this study, a 58-step absorption model for shock layer gases suggested by Sutton (ref. 14) is used. The expression for the net radiative flux in the shock layer usually is given by (ref. 2):

$$q_R = q_R^+ - q_R^- \tag{12}$$

where q_R^+ represents the energy transfer towards the shock and q_R^- the energy transfer towards the body. For the nonequilibrium case, the radiative heating to the body is calculated by using the nonequilibrium species concentration and an effective electronic temperature.

2.6. Thermodynamic and Transport Properties

Thermodynamic and transport properties are required for each species considered in the different flow regimes. Complete information for obtaining these properties is given in references 2 and 18.

3. METHOD OF SOLUTION

An iterative procedure has been used to couple the precursor and shock-layer solutions. The viscous shock-layer solutions are obtained by following the basic procedures suggested in references 15 to 18. The solution procedures for the precursor as well as shock-layer regions are described in reference 2.

4. RESULTS AND DISCUSSION

Information on Jupiter's atmospheric conditions is available in references 20 to 22. For different altitudes of entry, the free-stream conditions used in this study are given in references 1 and 2. The temperature of the atmosphere (i.e., T_∞) is taken to be 145 K. In the past, the nominal composition of the atmosphere was assumed to be 85 percent hydrogen and 15 percent helium by mole fraction. Recently, this has been changed to 89 percent hydrogen and 11 percent helium (ref. 22). Illustrative results have been obtained by using both of these compositions.

The entry body considered is a 45-degree hyperboloid blunt body which enters the Jovian atmosphere at a zero angle of attack. The body surface is assumed to be gray and have a surface emittance of 0.8. Unless specified otherwise, the surface temperature is taken to be uniform at 4,564 K. For the case of chemical equilibrium in the shock layer, all results were obtained by considering a body nose radius of $R_N^* = 23$ cm. For chemical nonequilibrium conditions, however, three different nose radii (12, 23, and 45 cm) were considered.

To illustrate the important features of the nonequilibrium analysis, most results were obtained for entry conditions which closely correspond to the peak heating conditions (i.e., for conditions at Z = 116 km). However, a few illustrative results have also been obtained for other entry conditions. Equilibrium and nonequilibrium results are presented first for variation of different properties in the shock layer. Results are then presented to illustrate the influence of precursor heating. Finally, results are presented for variation of different heat fluxes in the shock layer under the influence of both the nonequilibrium conditions and the precursor heating.

By considering initial composition of hydrogen species, just behind the shock, corresponding to both the "completely frozen" and "half frozen" conditions, nonequilibrium results were obtained for entry conditions at Z = 116 km and for 85 percent hydrogen nominal atmosphere. The results are illustrated in figures 2 to 4 as a function of the normal coordinate at the stagnation point. Figure 2 shows the mole concentration of different species across the shock layer. It is evident from this figure that molecular hydrogen is completely dissociated within about four percent of the total shock standoff distance from the shock wave. This is referred to as the dissociation zone (or the dissociated region). The variation in nondimensional v-velocity component and density is illustrated in figure 3. Since molecular weights change rapidly in the dissociated region, there is an increase in velocity and a decrease in density near the outer edge of the dissociation zone. The temperature distribution is shown in figure 4. It is noted that the temperature just behind the shock wave reaches a value of approximately 45,000 K in the completely frozen condition. After a short interval, however, all hydrogen molecules are dissociated and temperature drops to about 25,000 K. Next, ionization occurs and, as a result of this, temperature continues to decrease until it reaches the equilibrium value. From the results presented in figures 2 to 4, it is concluded that the half frozen and completely frozen assumptions are quite close except in the dissociated region near the shock wave, and that the half frozen flow computation is a reasonably good assumption for conditions of chemical nonequilibrium at altitudes near the peak heating region. Thus, all other results presented in this section have been obtained by considering only the half frozen conditions behind the shock.

As discussed in reference 2, the shock standoff distance (for a given body nose radius) varies with the altitude of entry and entry velocity. It should be pointed out here that, in general, the shock standoff distance increases as the body nose radius increases. For entry conditions at Z = 116 km, equilibrium and nonequilibrium results for the shock standoff distance are illustrated in figure 5 as a function of the coordinate along the body surface. It is noted that the shock standoff distances for equilibrium and with radiation are considerably lower than for nonequilibrium and with no radiation. This, however, would be expected because shock-layer densities are greater for radiation and equilibrium conditions than for no radiation and nonequilibrium conditions.

Variations in chemical species across the shock layer are shown in figures 6 to 9 for different conditions. For entry conditions at Z = 116 km, results presented in figures 6 and 7 show that the nonequilibrium layer is about 25 percent of the total shock-layer thickness for the no radiation case and about 50 percent for the case with radiation. This is because inclusion of radiation results in a different temperature distribution in the shock layer. This point will be discussed further while presenting results for the temperature variation. Near the wall, the mass fractions of atomic hydrogen and electrons are higher for nonequilibrium conditions with radiation. This is because cold gases near the wall absorb relatively more radiative heat flux in the nonequilibrium case. For the case of no radiation, a comparison of results presented in figures 6 and 8 reveals that the nonequilibrium layer increases from 25 percent at Z = 116 km to about 40 percent at Z = 143 km. This is because density is lower at higher altitudes and, therefore, it will take a relatively longer time to reach an equilibrium condition. For Z = 116 km entry conditions, figure 9 shows the species concentrations for 3 different body-nose radii (12, 23, and 45 cm). These results indicate that the thickness (or range) of the nonequilibrium layer decreases with increasing nose radius. In particular, it is seen that the thickness is about 40 percent for R_n^* = 12 cm, but it is only 10 percent for R_n^* = 43 cm. This is because the shock standoff distance is proportional to the body nose radius and the relaxation time for chemical reactions is about the same for all cases.

For entry conditions at Z = 116 km, absorption coefficients of the shock-layer gas were calculated under equilibrium and nonequilibrium conditions. Results obtained for conditions at a location in the shock layer, which is at 10 percent of the shock standoff distance from the shock wave, are illustrated in figure 10 as a function of electron-volts. The figure exhibits the trend that is quite typical of results for other conditions. It is seen that the nonequilibrium absorption is considerably higher than the equilibrium absorption for most parts of the spectral range. As such, one would except relatively larger radiative heating of the entry body under nonequilibrium conditions.

Temperature distributions across the shock layer are illustrated in figures 11 to 13 for different conditions. For the case with no radiation,

the heavy particle and electron temperature variations across the shock layer are illustrated (along with the equilibrium temperature distribution) in figure 11 for different entry conditions. The results show that, in the absence of radiation, the nonequilibrium temperature is higher than the equilibrium temperature throughout the shock layer for each entry condition. It is also noted that the electron temperature, which is lower than the heavy particle temperature during early stages of ionization, asymptotically approaches the heavy particle temperature during the later stages of ionization. As discussed in the previous section, the temperature distribution in the shock layer is relatively higher for higher altitudes because of higher entry velocities. For entry conditions at Z = 116 km, the electron temperature distributions (without and with radiation) are shown in figures 12 and 13 for 3 different body nose radii. As noted earlier, the thickness of the nonequilibrium layer decreases with increasing nose radius. Also, for a given nose radius, inclusion of radiation increases the thickness of the nonequilibrium layer. This is because the loss of radiation from the shock layer results in an entirely different temperature distribution (see fig. 13) and leaves relatively less energy for dissociation and ionization of the gas.

For entry conditions at Z = 116 km, figure 14 shows the mass fraction of atomic hydrogen and hydrogen ion along the stagnation streamline in the precursor region. While equilibrium results indicate that only 5 percent hydrogen is dissociated and 0.018 percent is ionized, the nonequilibrium results show that 15 percent hydrogen is dissociated and 0.8 percent ionized. It should be pointed out that the composition of the precursor gas will be different for different entry conditions. It should be emphasized here again that in investigating the precursor region flow properties and their influence on the shock-layer flow phenomena, the entire precursor-shock layer solutions are obtained by iterative procedures.

For the case with radiation and for entry conditions at Z = 116 km, the heavy particle and electron temperature variations across the shock layer are illustrated in figure 15 along with the equilibrium temperature distribution. In comparison with results of figure 11, it is seen that in the present case the nonequilibrium temperature is lower than the equilibrium temperature in certain portions of the shock. This is a direct consequence of the radiation cooling (i.e., radiation loss to the free stream) of the

shock layer. Also, in this case the nonequilibrium temperature is slightly higher than the equilibrium temperature in the vicinity of the wall. This is because cold gases near the wall absorb radiation from the high-temperature region of the shock layer. As would be expected, precursor heating results in a slightly higher shock-layer temperature distribution.

Variations of temperature, pressure, and density along the stagnation streamline in the entire shock layer-precursor zone are illustrated in figures 16 to 19 for different conditions. These results show that precursor effects are higher for the nonequilibrium conditions. This, however, would be expected since, in this case, the radiative heat flux toward the precursor region is considerably higher. The shock-layer nonequilibrium condition significantly influences the temperature and pressure variations in the precursor zone, but its effects on density changes are quite small. As noted earlier, in the shock layer, nonequilibrium results approach the corresponding equilibrium values at about 25 percent of the shock-layer thickness from the shock wave. For the equilibrium case, the influence of precursor heating on shock-layer temperature, pressure, and density variations is discussed in reference 2.

For a comparison of the shock-layer flow phenomena for the two nominal compositions of the Jovian atmosphere, illustrative results were obtained for entry conditions at Z = 116 km. Results for the temperature variation immediately behind the shock and for the radiative heat flux across the shock layer are illustrated in figures 20 to 22. It is evident from figure 20 that the shock temperature is lower by about 2 percent for case of the 89 percent hydrogen atmosphere. This is because, in this case, relatively more energy is required to dissociate the molecular hydrogen. Since the shock temperature is lower in this case, the radiative heat fluxes (q^+ as well as q^-) are lower for both equilibrium and nonequilibrium conditions (see figs. 21 and 22).

To investigate the extent of heating on an entry body, the variations in radiative heat flux in the shock layer were calculated for different conditions. As discussed earlier, the chemical nonequilibrium effects are more important with small body nose radius and for higher altitude entry conditions. Results for radiative flux toward the shock and body are shown in figure 23 for R_n^* = 12 cm and Z = 116 km. The results indicate that, in

the nonequilibrium case, the radiative heat flux is increased to about 70 percent toward the body and almost 2.5 times toward the shock (i.e., toward the precursor region). Results for radiative heating of the body for $R_n^* = 23$ cm and $Z = 143$ km are shown in figure 24. The results show that the heat flux is about three times higher for nonequilibrium conditions. This is a direct consequence of the higher temperature in the nonequilibrium layer near the shock.

To investigate the influence of precursor heating on viscous, nonequilibrium, shock-layer flow phenomena, specific results were obtained for the peak heating entry conditions and for an entry body with a nose radius of $R_n^* = 23$ cm. These are presented here as final results of the present study.

The radiative heat flux from the shock layer toward the shock front and the precursor region is shown in figure 25 for both equilibrium and nonequilibrium conditions. The results clearly indicate that heat flux toward the precursor region is considerably higher for nonequilibrium conditions. This is again a direct consequence of higher nonequilibrium temperature in the shock layer. As discussed before, precursor heating results in a higher radiative flux at the shock front. The results of figure 25 indicate that precursor heating results in a 15 percent increase in radiative flux in the nonequilibrium case while only 8.5 percent increase is noticed for the equilibrium condition.

The results of equilibrium and nonequilibrium radiative flux toward the body (along the stagnation line) are illustrated in figure 26. Although it is realistic to calculate the radiative flux based on the electron temperature, results (for the case with no precursor effects) have been obtained also by using the heavy particle temperature only for comparative purposes. The nonequilibrium results are seen to be significantly higher than the equilibrium results. This is primarily due to the high-temperature region near the shock where nonequilibrium temperature overshoots occur.

Figure 27 shows the variation of radiative and convective flux with distance along the body surface. The radiative as well as convective heat transfer to the body surface is seen to be enhanced by the nonequilibrium conditions. As discussed above, the increase in radiative heating is a direct consequence of higher electronic temperature. For the case with no

radiation, the convective heat flux toward the body was found to be the same for equilibrium and nonequilibrium conditions. For the case with radiation, however, figure 27 shows that the convective heat flux for the nonequilibrium case is about 20 percent higher than the corresponding equilibrium value at the stagnation point. This is because the cold gas near the wall absorbs higher radiative flux from the shock layer under the nonequilibrium conditions. As discussed before, the influence of precursor heating is enhanced due to nonequilibrium conditions. Figure 27 shows that precursor heating results in a 10.5 percent increase in the radiative flux at the stagnation point in the nonequilibrium case while only about 7 percent increase is noted for the equilibrium case.

For the entry conditions considered in this study, therefore, it is logical to conclude that nonequilibrium heating of the body is significantly higher than equilibrium heating. Results similar to this were also obtained by Grose and Nealy (ref. 10) for Venusian entry conditions. For certain Jovian entry conditions, results presented in references 3 to 6 indicate that nonequilibrium heating is considerably less than the equilibrium heating. This obviously is in contradiction to the present findings. It should be pointed out that for the entry conditions considered in this study, the temperature just behind the shock is very high and all hydrogen molecules are completely dissociated. Under these conditions, H_β line emissions are higher than for the equilibrium conditions. This is because, in addition to high temperature, the number density of atomic hydrogen is considerably higher than the equilibrium value. Thus, findings of the present study appear to be completely justified.

5. CONCLUSIONS

The results of present investigation reveal that there exists a nonequilibrium layer of considerable thickness in the shock layer. Since dissociation reactions occur only within a very short distance from the shock wave, it is reasonable to assume that all hydrogen molecules are dissociated (half frozen condition) immediately behind the shock. The thickness of the nonequilibrium layer increases with increasing altitudes, decreasing body nose radius, and with inclusion of the radiative heat-flux term in the energy equation.

Under nonequilibrium conditions, temperature (heavy particle as well as electronic) overshoots occur near the shock wave. As a result of this, the radiative as well as convective heat transfer to the body surface is increased significantly. The influence of precursor heating is enhanced due to nonequilibrium conditions: a 9.5 percent increase in the stagnation point radiative heating has been observed at an altitude of 116 km.

REFERENCES

1. Tiwari, S.N.; and Szema, K.Y.: Radiation Induced Precursor Flow Field Ahead of a Jovian Entry Body. NASA TR NAS1-11707-92, Apr. 1977; also AIAA Paper No. 77-768, June 1977.

2. Tiwari, S.N.; and Szema, K.Y.: Influence of Precursor Heating on Viscous Flow Around a Jovian Entry Body. AIAA Paper No. 78-190, Jan. 1978; also NASA TR NAS1-14193-27, Sept. 1978.

3. Leibowitz, L.P.: Measurement of the Structure of an Ionizing Shock Wave in a Hydrogen-Helium Mixture. Phys. Fluids, Vol. 16, No. 1, Jan. 1973, pp. 59-68.

4. Howe, J.T.: Hydrogen Ionization in the Shock Layer for Entry into the Outer Planets. AIAA, Vol. 12, No. 6, June 1974, pp. 875-876.

5. Leibowitz, L.P.: Jupiter Entry Simulation with the ANAA Shock Tube. AIAA Paper No. 74-610, July 1974.

6. Leibowitz, L.P.; and Kuo, T.J.: Outer Planet Nonequilibrium Heating. AIAA Paper No. 75-1149, Sept. 1975; also AIAA, Vol. 8, No. 9, Sept. 1976, pp. 1324-1329.

7. Teare, J.D.; Georgiev, S.; and Allen, R.A.: Radiation From the Nonequilibrium Shock Front. Report No. 112, AVCO-Everett Research Lab. (Everett, Mass.), Oct. 1961.

8. Hansen, C.F.; and Chapin, C.E.: Nonequilibrium Radiation from the Stagnation Region of High-Velocity Bodes. Report No. TR 64-02G, General Motors Defense Research Labs. (Santa Barbara, Calif.), Aug. 1964.

9. Page, W.A.; and Arnold, J.O.: Shock Layer Radiation of Blunt Bodies at Reentry Velocities. NASA TR R-193, 1964.

10. Grose, W.L.; and Nealy, J.E.: Estimates of Nonequilibrium Radiation for Venus Entry. AIAA, Vol. 13, No. 4, Apr. 1975, pp. 421-424.

11. Zoby, E.V.; Gnoffo, P.A.; and Graves, R.A.: Correlations for Determining Thermodynamic Properties of Hydrogen-Helium Gas Mixtures at Temperatures from 7,000 to 35,000 K. NASA TN D-8262, Aug. 1976.

12. Vincenti, W.G.; and Kruger, C.H.: Introduction to Physical Gas Dynamics. John Wiley and Sons, 1965.

13. Horton, T.E.; and Menard, W.A.: A Program for Computing Shock Tube Gasdynamic Properties. Technical Report No. 32-1350, Jet Propulsion Laboratory (Pasadena, Calif.), 1969; also Phys. Fluids, Vol. 14; 1971, p. 1347.

14. Zoby, E.V.; Sutton, K.; Olstad, W.B.; and Moss, J.N.: An Approximate Inviscid Radiating Flow Field Analysis for Outer Planet Entry Probes. AIAA Paper No. 78-189, Jan. 1978.

15. Blottner, F.G.: Viscous Shock Layer at the Stagnation Point with Nonequilibrium Air Chemistry. AIAA, Vol. 7, No. 12, Dec. 1969, pp. 2281-2288.

16. Blottner, F.G.: Finite Difference Methods of Solution of the Boundary Layer Equations. AIAA, Vol. 8, No. 2, Feb. 1970, pp. 193-205.

17. Davis, R.T.: Numerical Solution of the Hypersonic Viscous Shock-Layer Equations. AIAA, Vol. 8, May 1970, pp. 843-851; also: Hypersonic Flow of a Chemically Reacting Binary Mixture Past a Blunt Body, AIAA Paper No. 70-805, June 1970.

18. Moss, J.N.: Reacting Viscous-Shock-Layer Solutions with Multicomponent Diffusion and Mass Injection. NASA TR R-411, June 1974.

19. Appleton, J.P.; and Bray, K.N.C.: The Conservation Equations for a Nonequilibrium Plasma. J. Fluid Mech., Vol. 20, Part 4, Dec. 1964, pp. 659-672.

20. Anon.: The Planet Jupiter. NASA Report SP-8069, Dec. 1971.

21. Moss, J.N.; Anderson, E.C.; and Bolz, C.W.: Aerothermal Environment for Jovian Entry Probes. AIAA Paper No. 76-469, June 1976.

22. Sutton, K.; Jones, J.J.; and Powell, R.W.: Effects of Atmospheric Structure on Radiative Heating for Jupiter Entry Probe. AIAA Paper No. 78-185, Jan. 1978.

Table 1. Reaction scheme and rate constants.

	Reactions	Rate constants in $cm^3\ sec^{-1}$
1.	$H + e \rightleftarrows H^+ + 2e$	$k_1 = 2.27E13\ T_e^{1/2} \exp(-1.578E5/T_e)$
2.	$He + e \rightleftarrows He^+ + 2e$	$k_2 = 1.33E13\ T_e^{1/2} \exp(-2.852E5/T_e)$
3.	$H + e \rightleftarrows H^* + e$, $H^* + e \rightleftarrows H^+ + 2e$	$k_3 = 4.11E13\ T_e^{1/2} \exp(-1.160E5/T_e)$
4.	$He + e \rightleftarrows He^* + e$, $He^* + e \rightleftarrows He^+ + 2e$	$k_4 = 2.24E13\ T_e^{1/2} \exp(-2.320E5/T_e)$
5.	$H + H \rightleftarrows H^* + H$, $H^* + H \rightleftarrows H^+ + e + H$	$k_5 = 6.20E10\ T^{1/2} \exp(-1.160E5/T)$
6.	$H + He \rightleftarrows H^* + He$, $H^* + He \rightleftarrows H^+ + e + He$	$k_6 = 4.89E10\ T^{1/2} \exp(-1.160E5/T)$
7.	$H_2 + He \rightleftarrows H + H + He$	$k_7 = 4.33E18\ T^{-1} [1-\exp(-1.5E8/T^2)] \exp(-52340/T)$
8.	$H_2 + H_2 \rightleftarrows H + H + H_2$	$k_8 = 2.5\ k_7$
9.	$H_2 + H \rightleftarrows H + H + H$	$k_9 = 14.0\ k_7$
10.	$H_2 + H^+ \rightleftarrows H + H + H^+$	$k_{10} = k_9$
11.	$H_2 + e \rightleftarrows H + H + e$	$k_{11} = k_9$

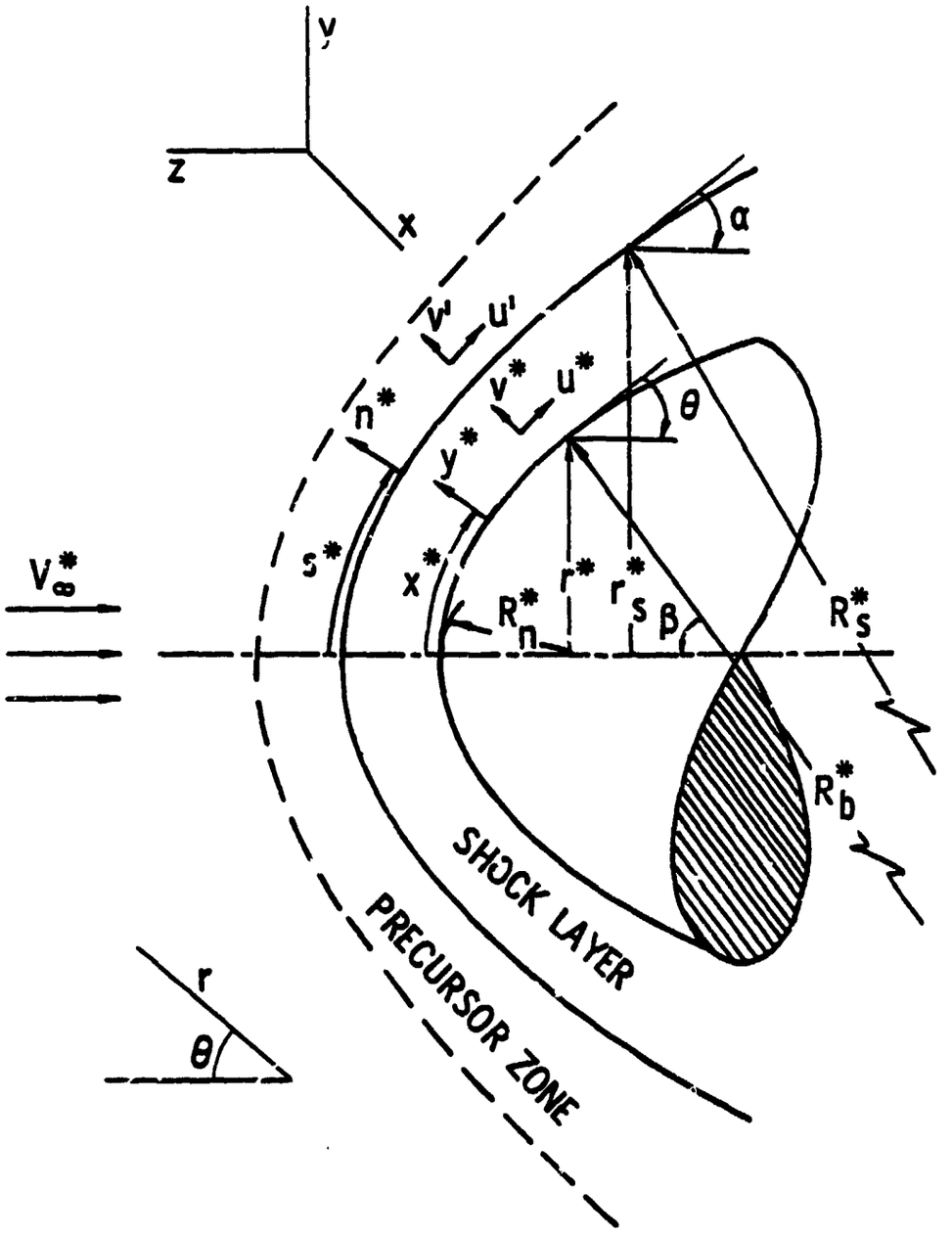

Figure 1. Physical model and coordinate system for a Jovian entry body.

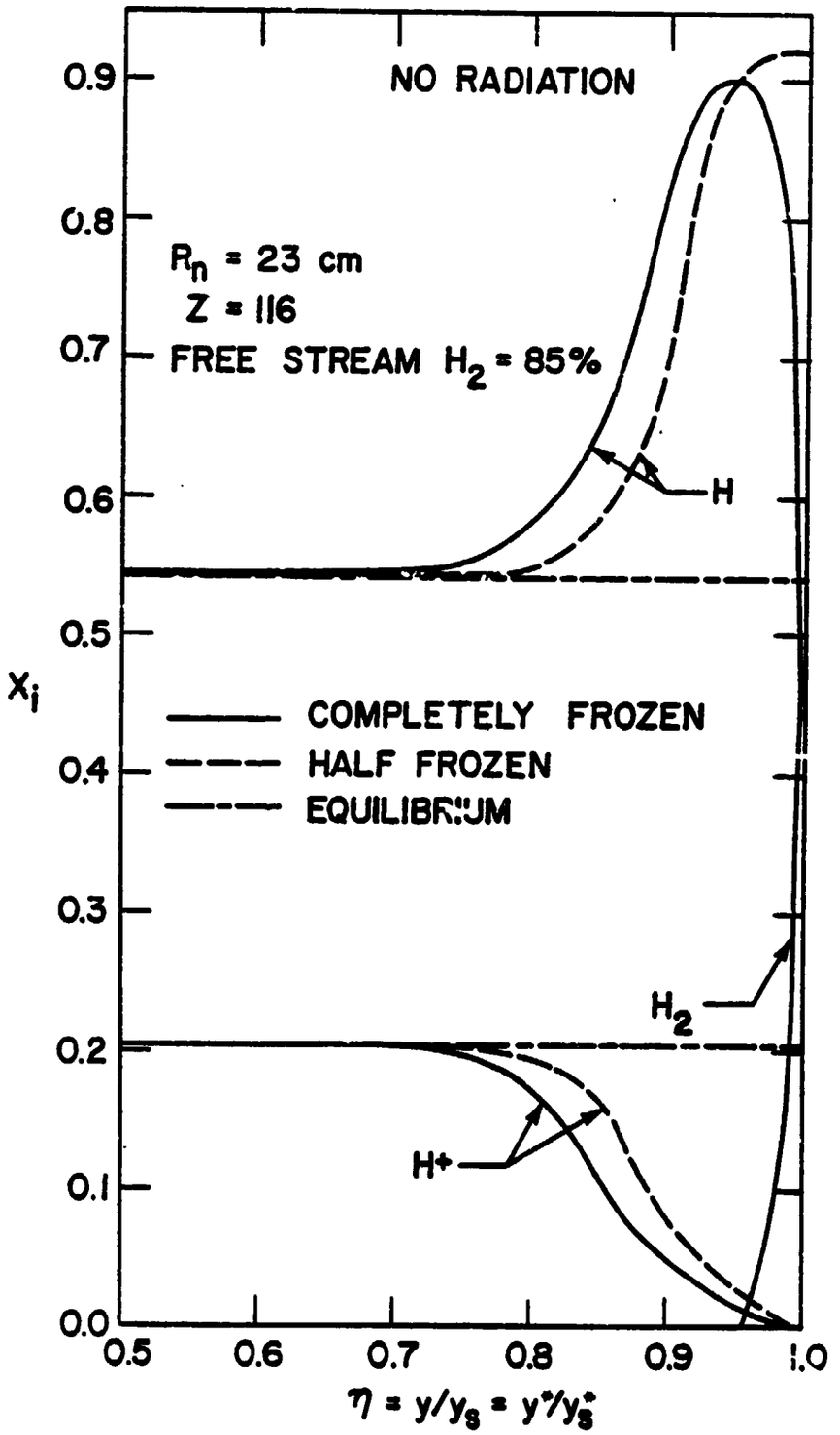

Figure 2. Species concentration variation in nonequilibrium shock-layer region for $\xi = 0$.

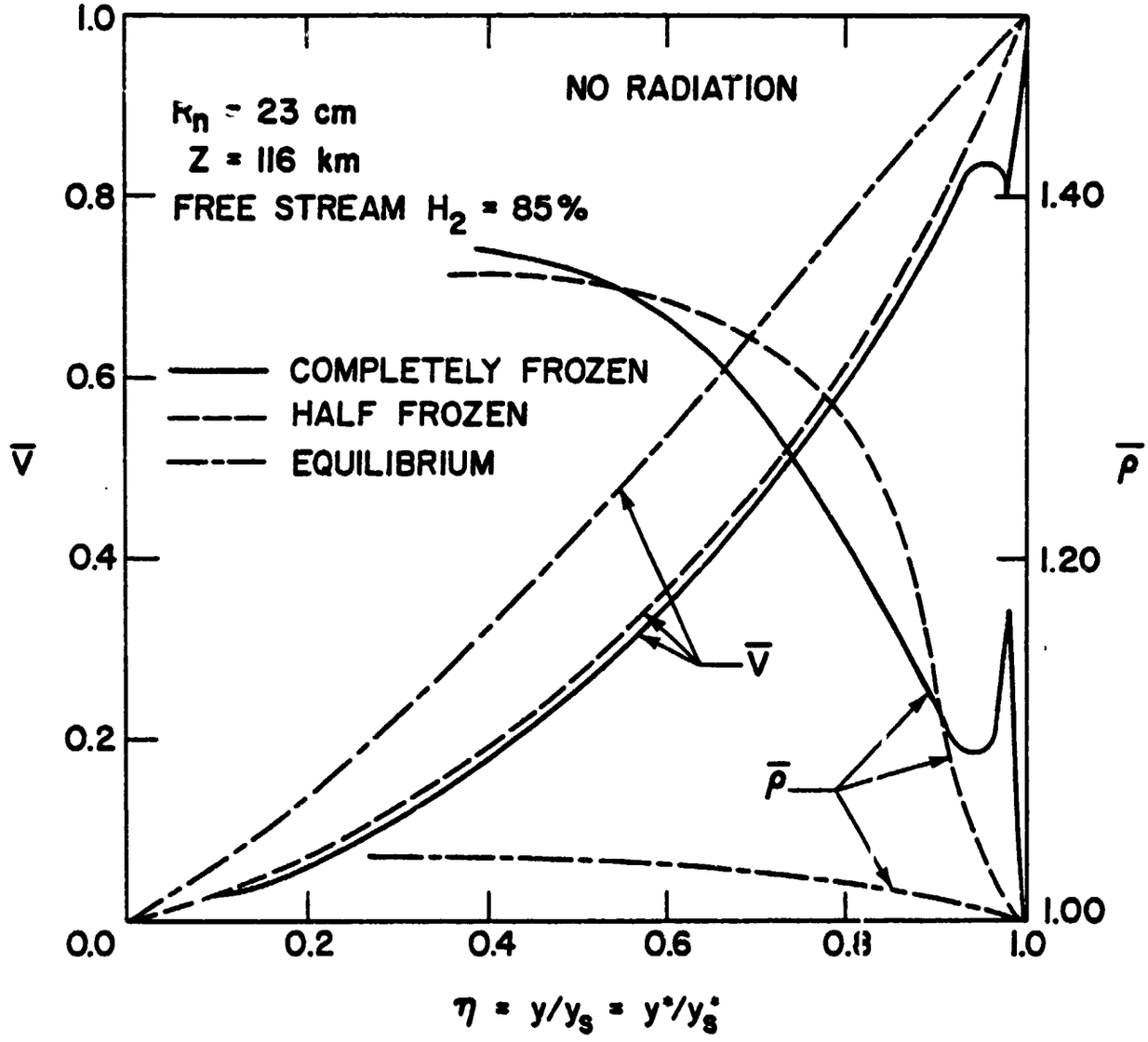

Figure 3. Equilibrium and nonequilibrium $\bar{v}$-velocity component and density variation in the shock layer for $\xi = 0$.

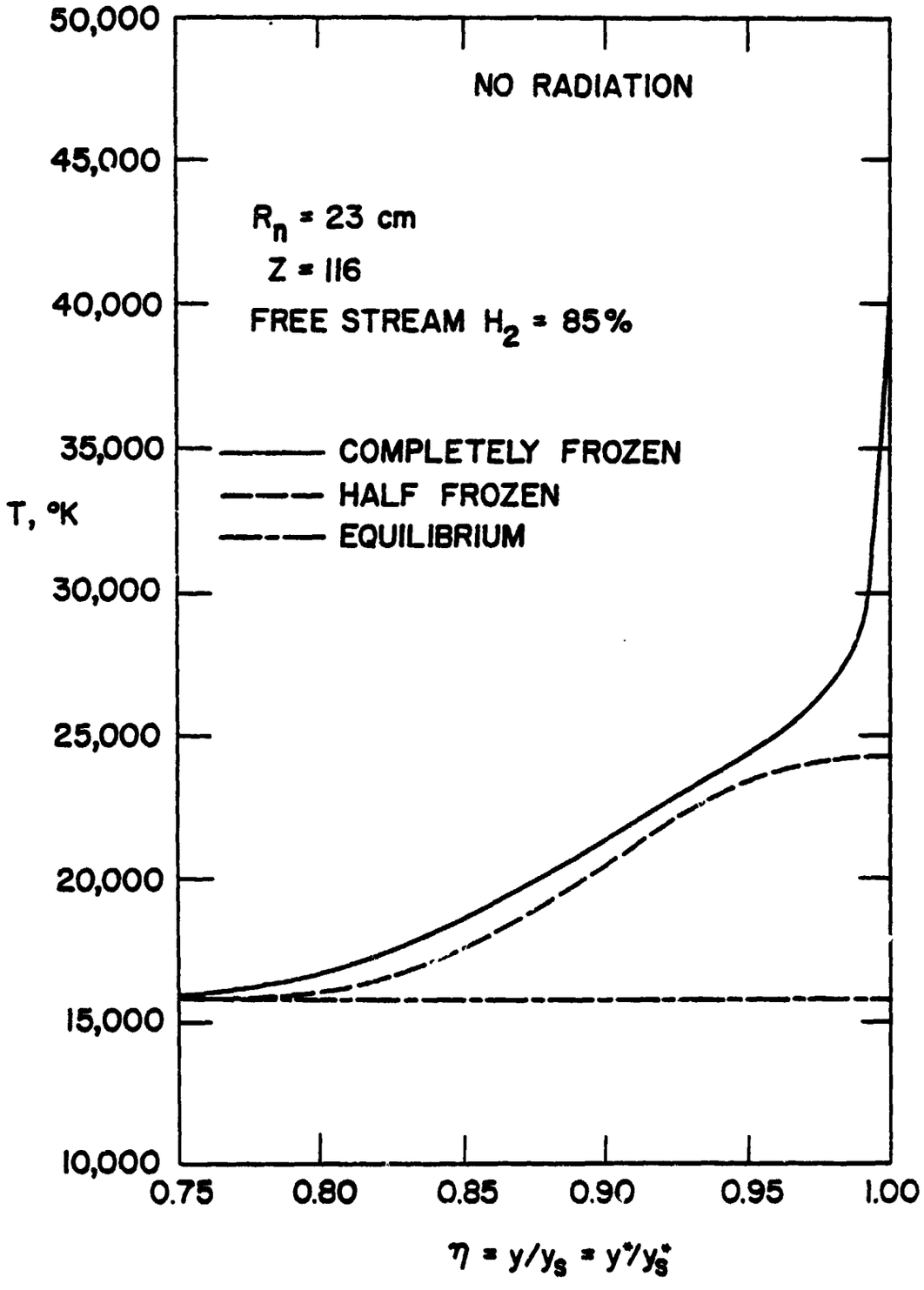

Figure 4. Temperature variation in nonequilibrium shock-layer region for $\xi = 0$.

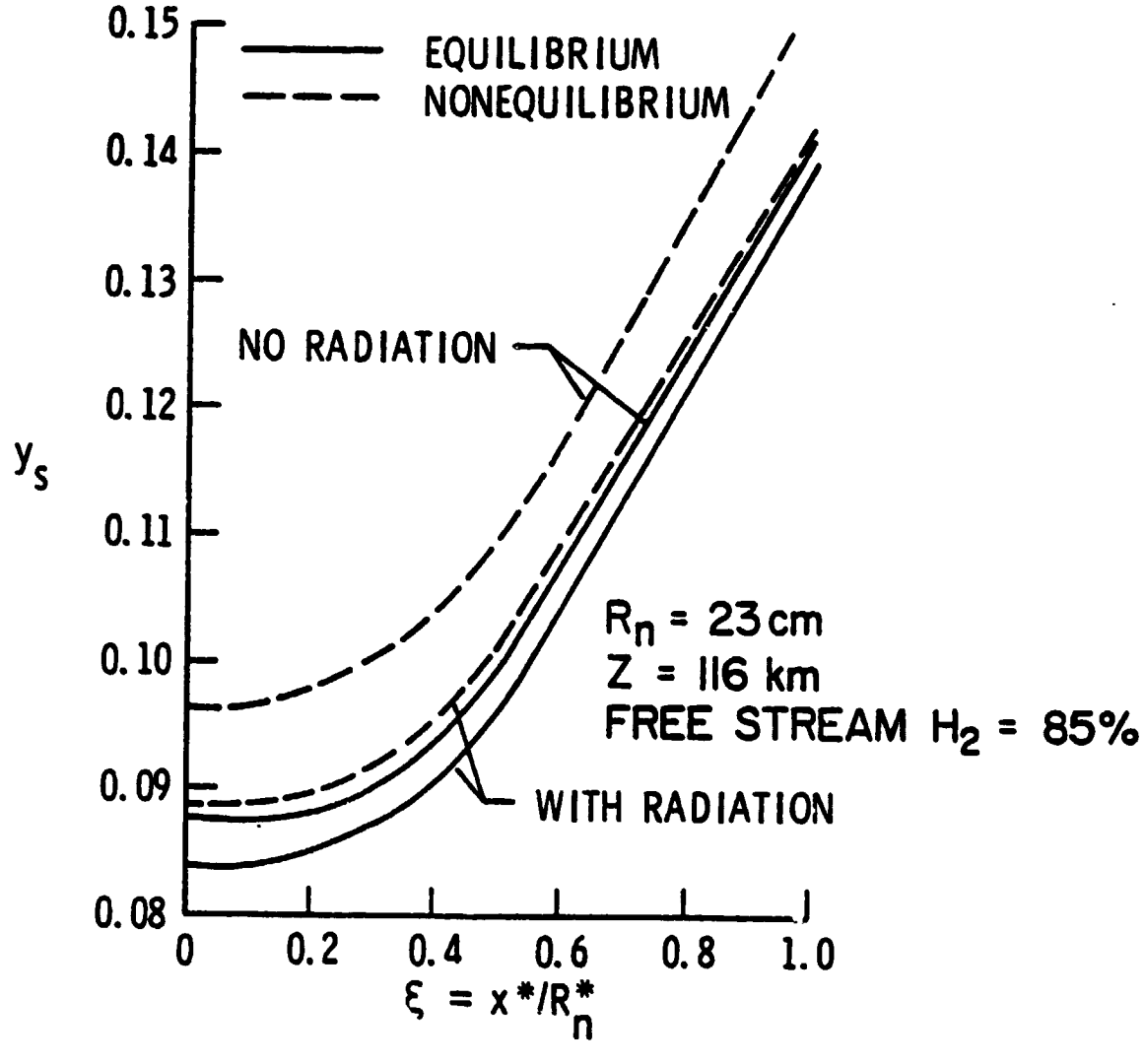

Figure 5. Shock-standoff variation with distance along the body surface.

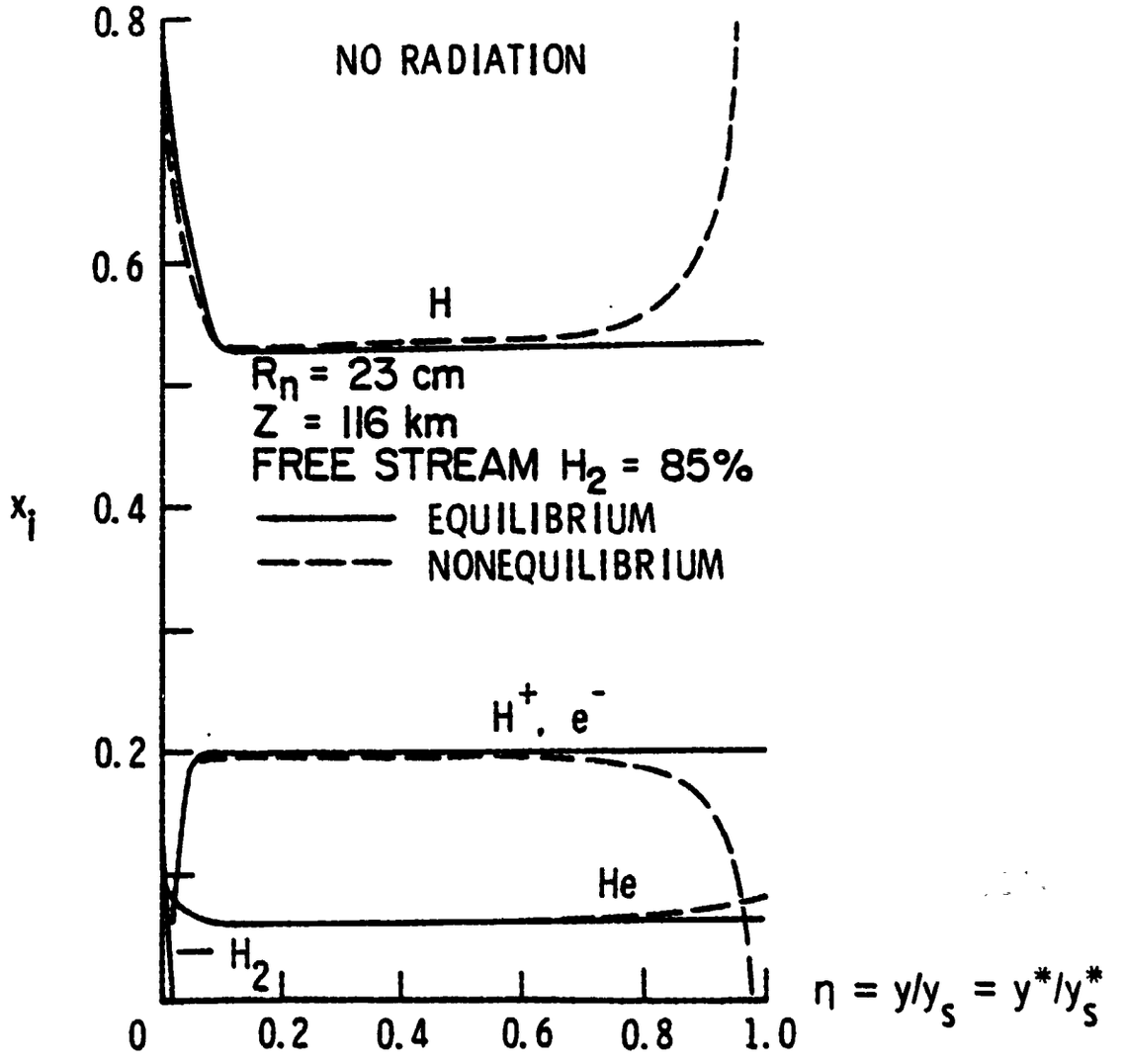

Figure 6. Species concentration in the shock layer for $\xi = 0$ (with no radiation).

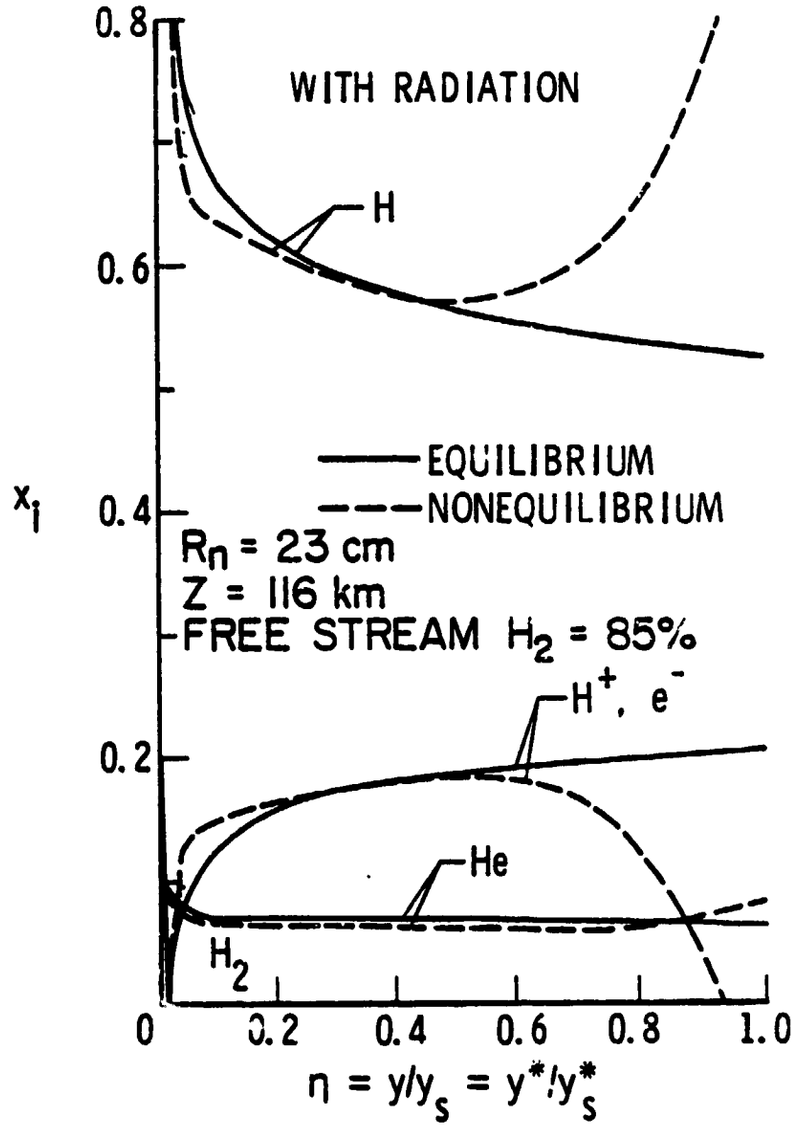

Figure 7. Species concentration in the shock layer for $\xi = 0$ (with radiation).

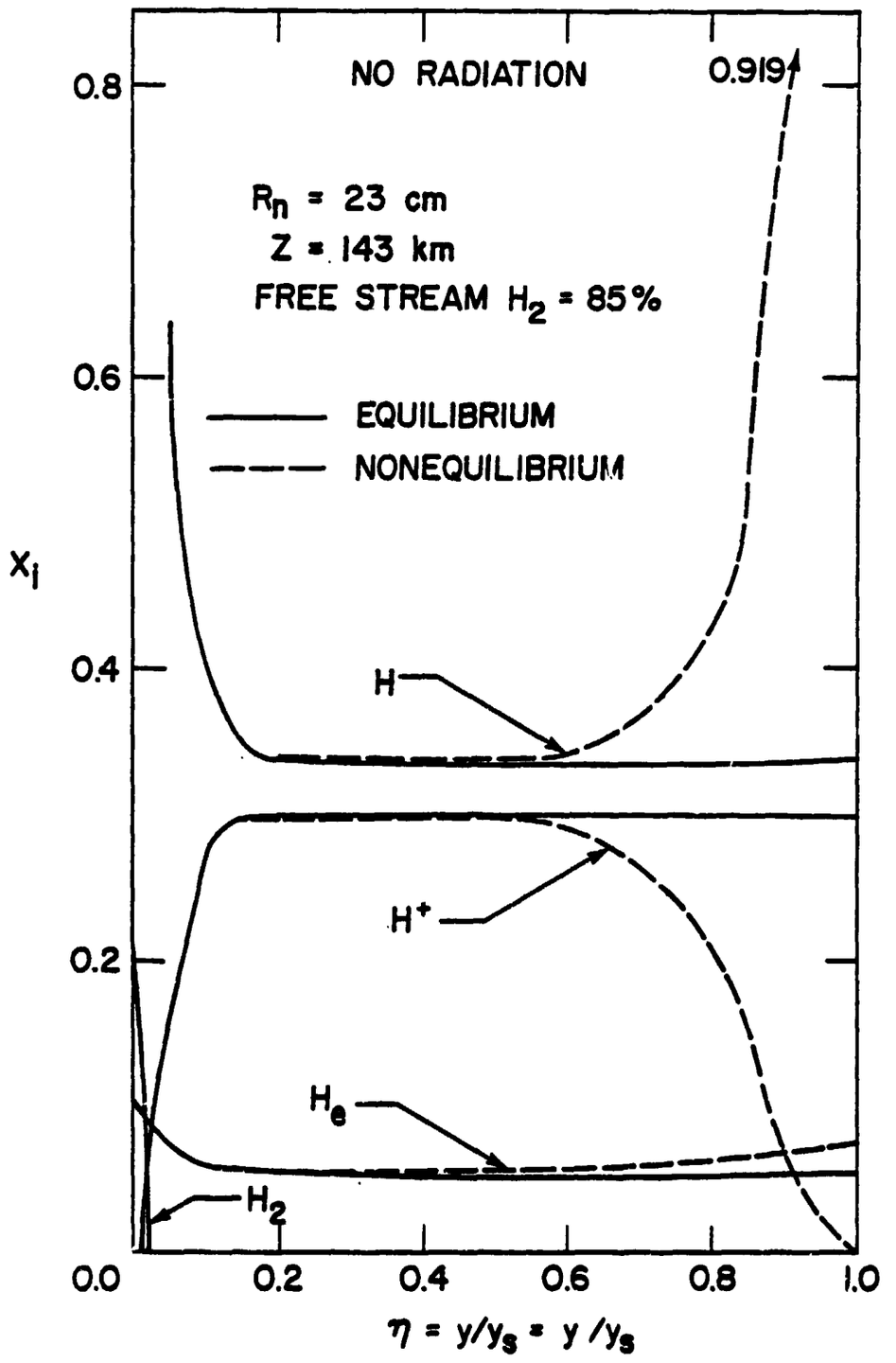

Figure 8. Species concentration in shock layer for $\xi = 0$ at $Z = 143$ km (with no radiation).

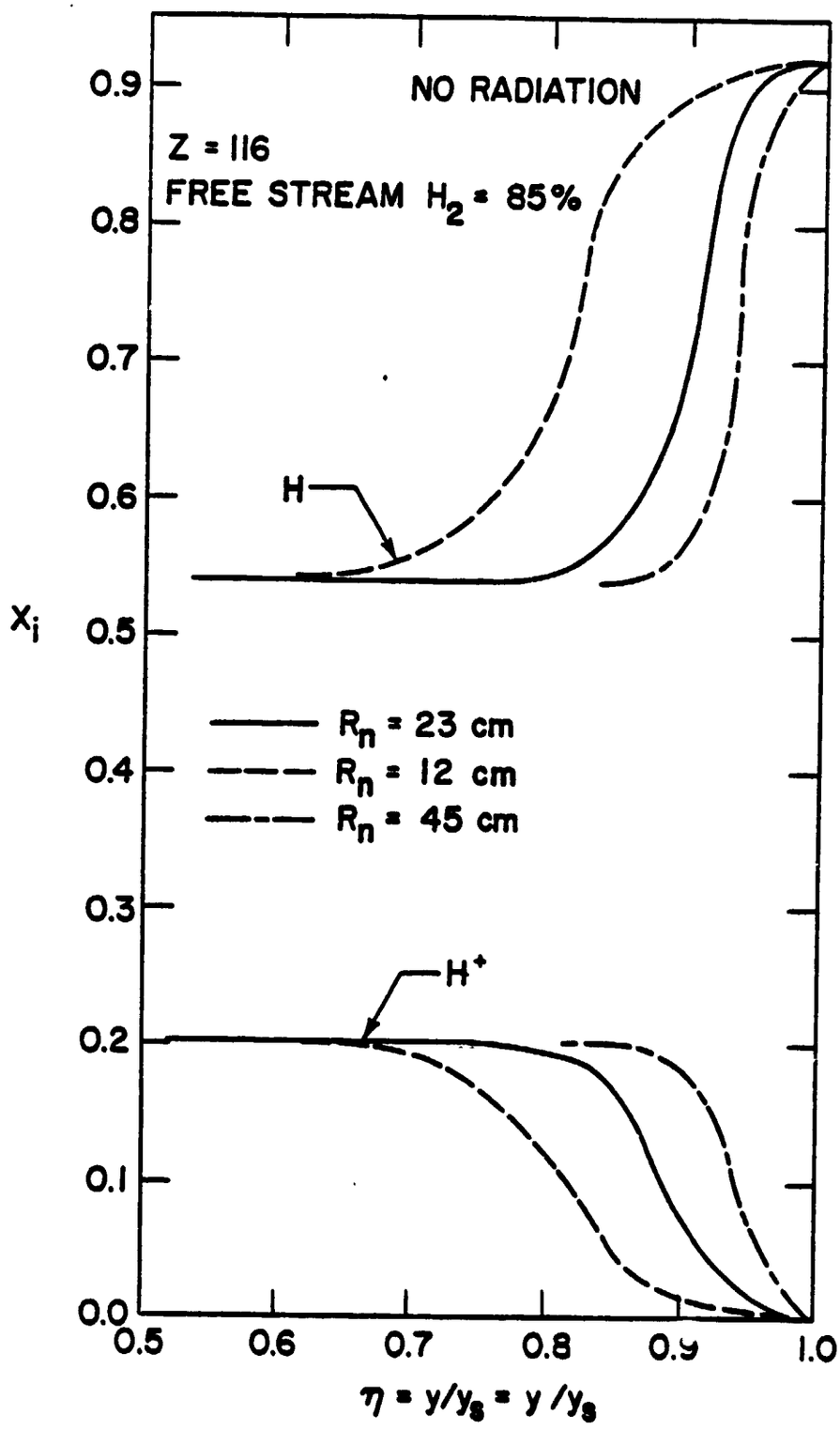

Figure 9. Species concentration for different body radius in the shock layer for $\xi = 0$ at $Z = 116$ km (with no radiation).

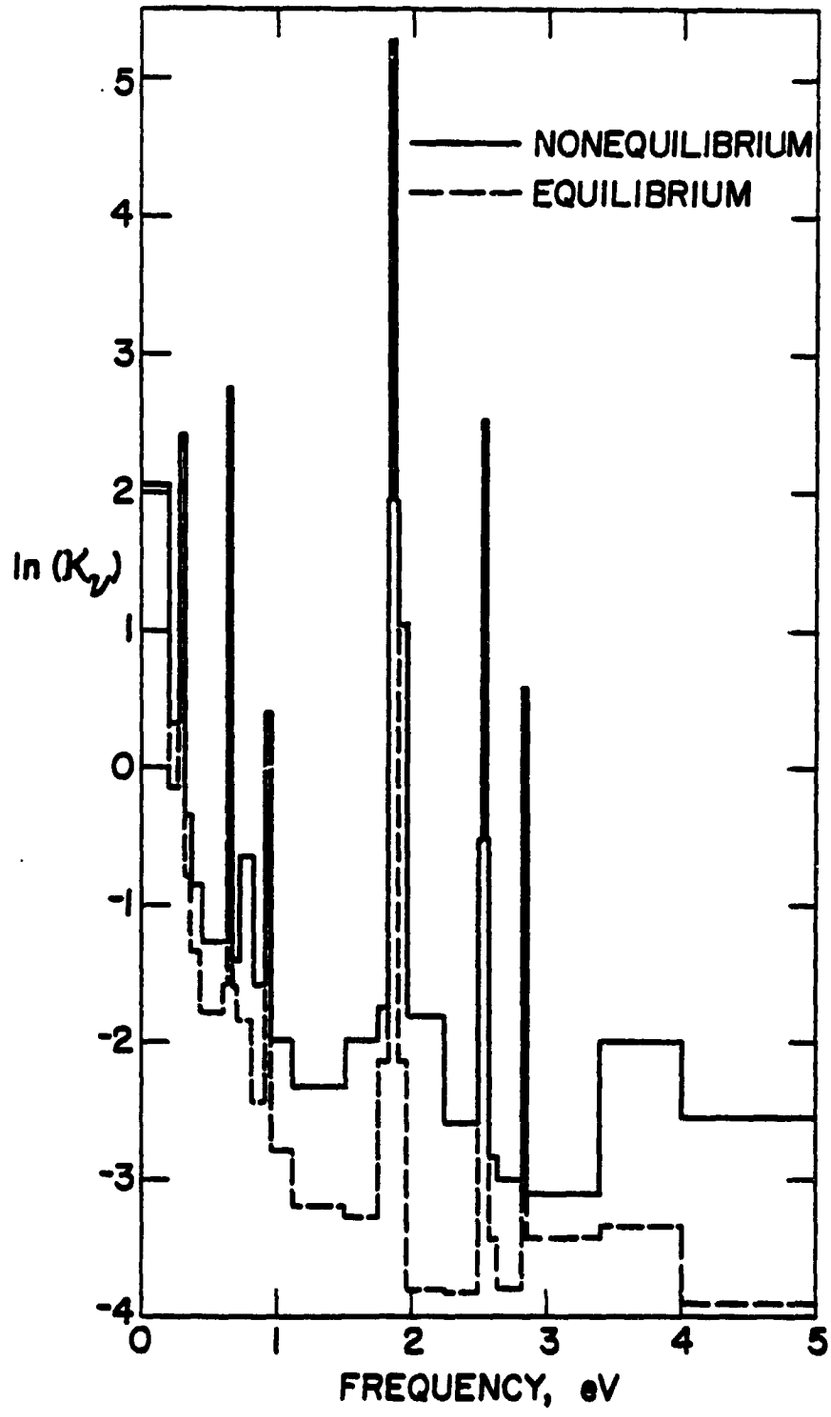

Figure 10(a). Variation of absorption coefficient for equilibrium and nonequilibrium conditions in the shock layer, Z = 116 km.

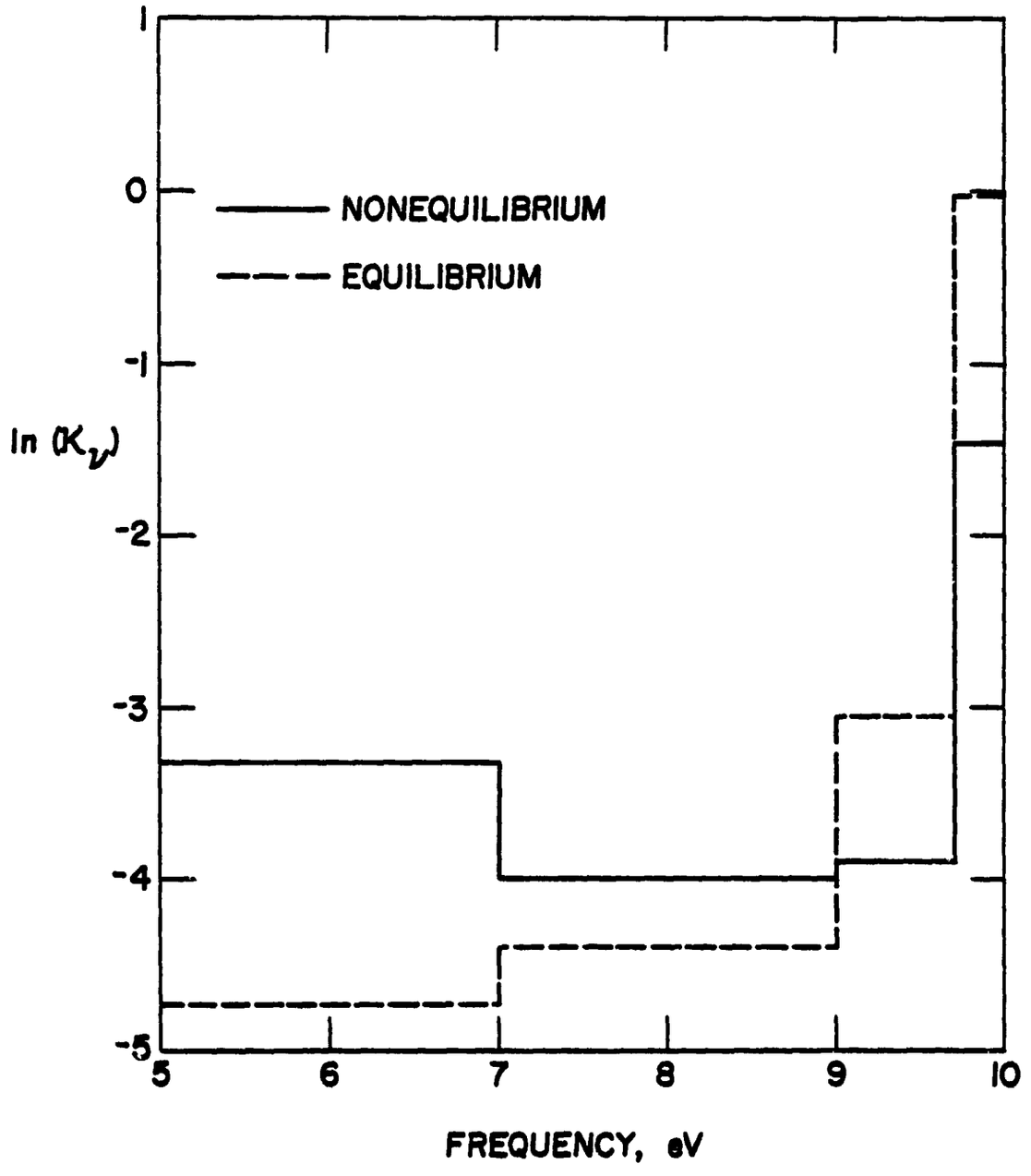

Figure 10(b). Variation of absorption coefficient for equilibrium and nonequilibrium conditions in the shock layer, Z = 116 km.

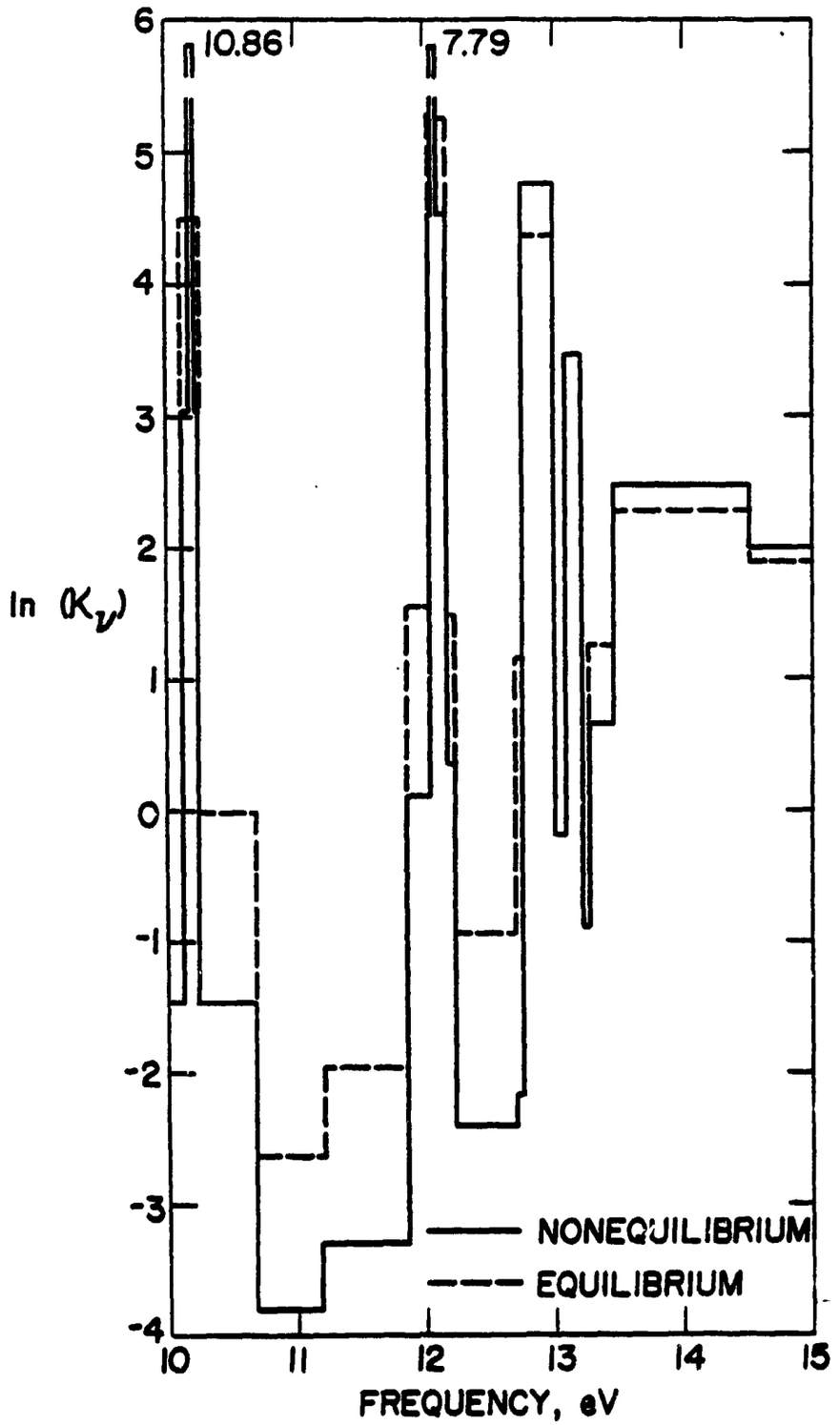

Figure 10(c). Variation of absorption coefficient for equilibrium and nonequilibrium conditions in the shock layer, Z = 116 km.

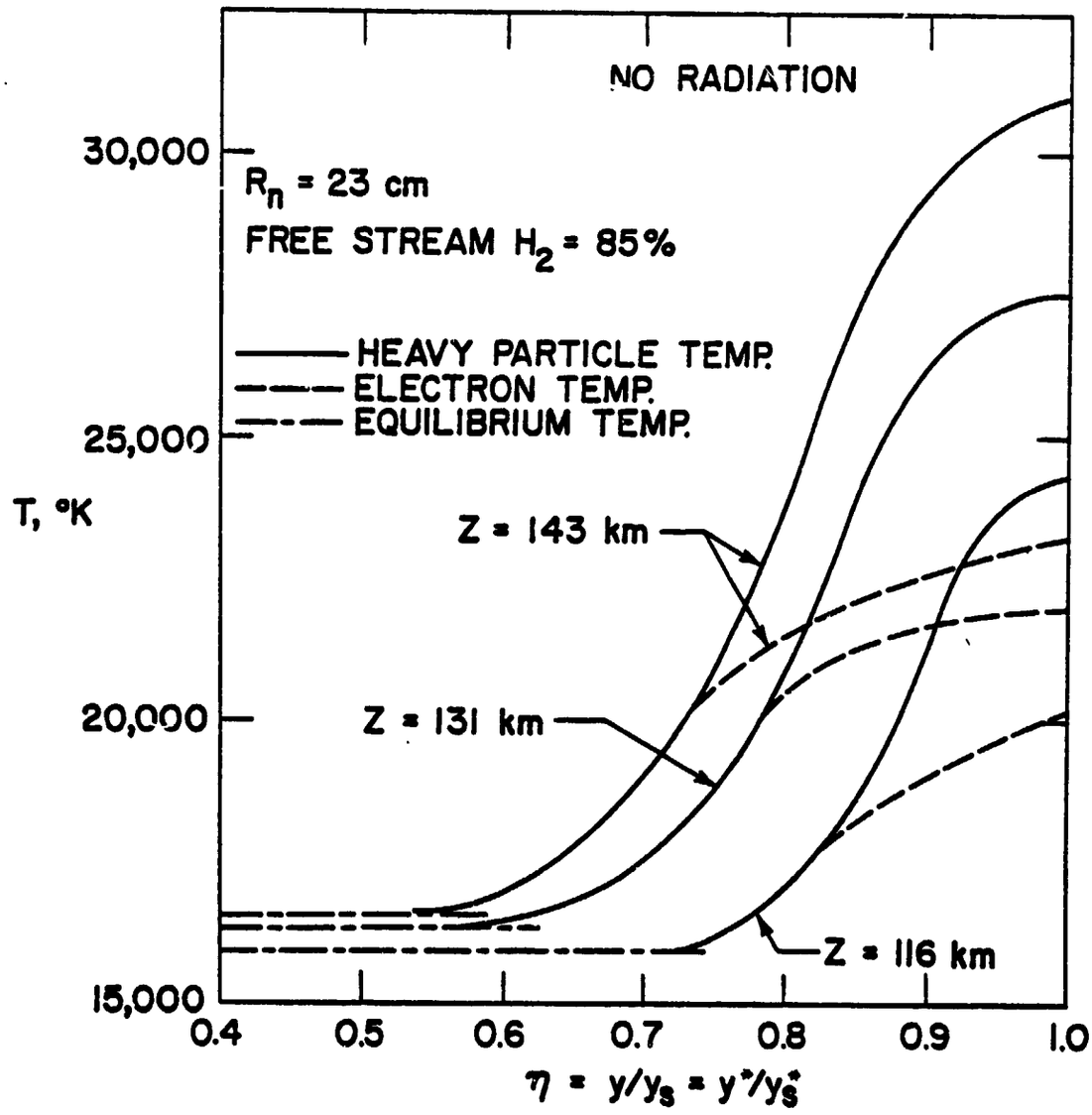

Figure 11. Heavy particle and electron temperature variation in the shock-layer nonequilibrium region.

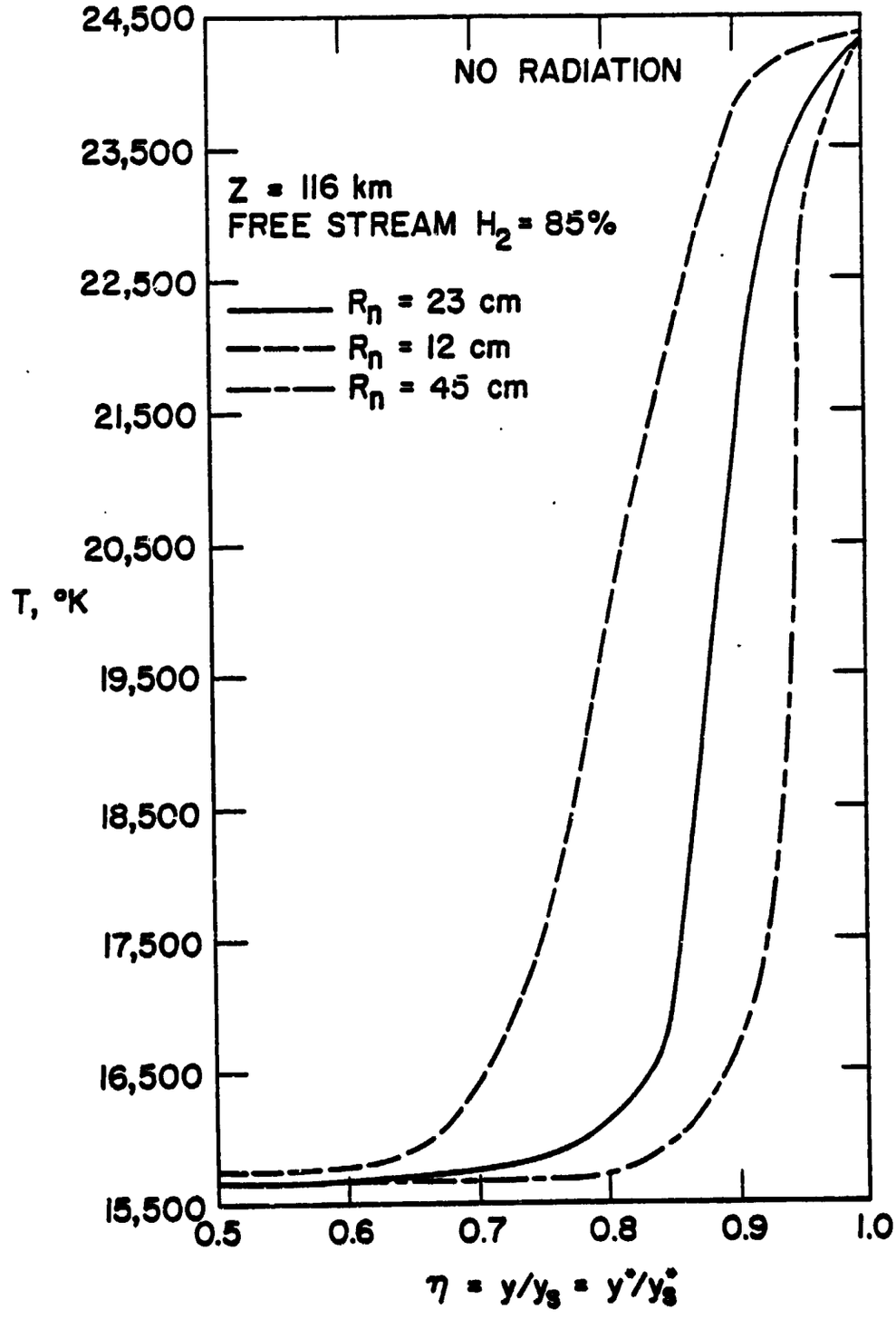

Figure 12. Temperature variation for different body nose radius in the nonequilibrium region at $\xi = 0$ (with no radiation).

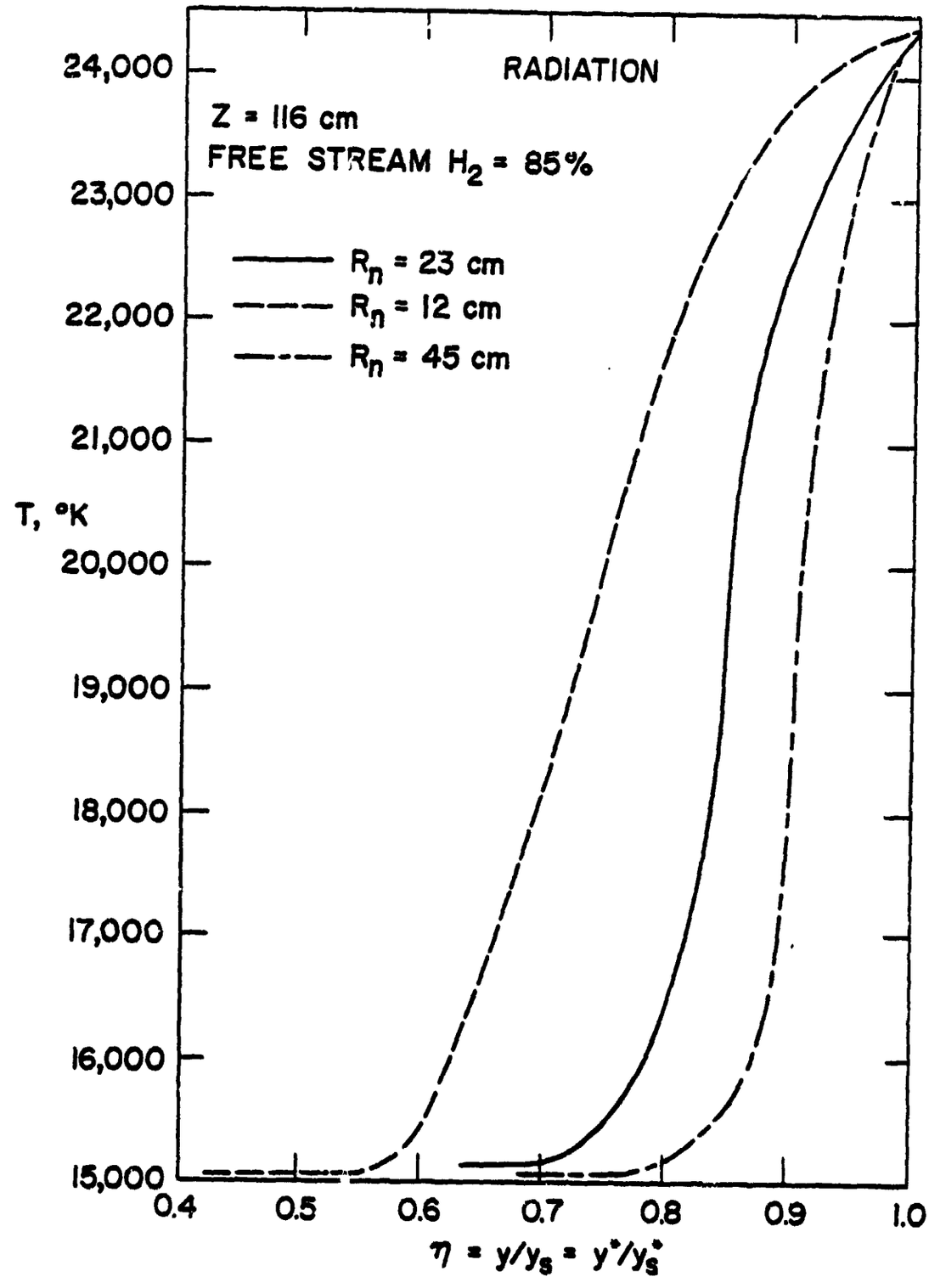

Figure 13. Temperature variation for different body nose radius in the nonequilibrium region at $\xi = 0$ (with radiation).

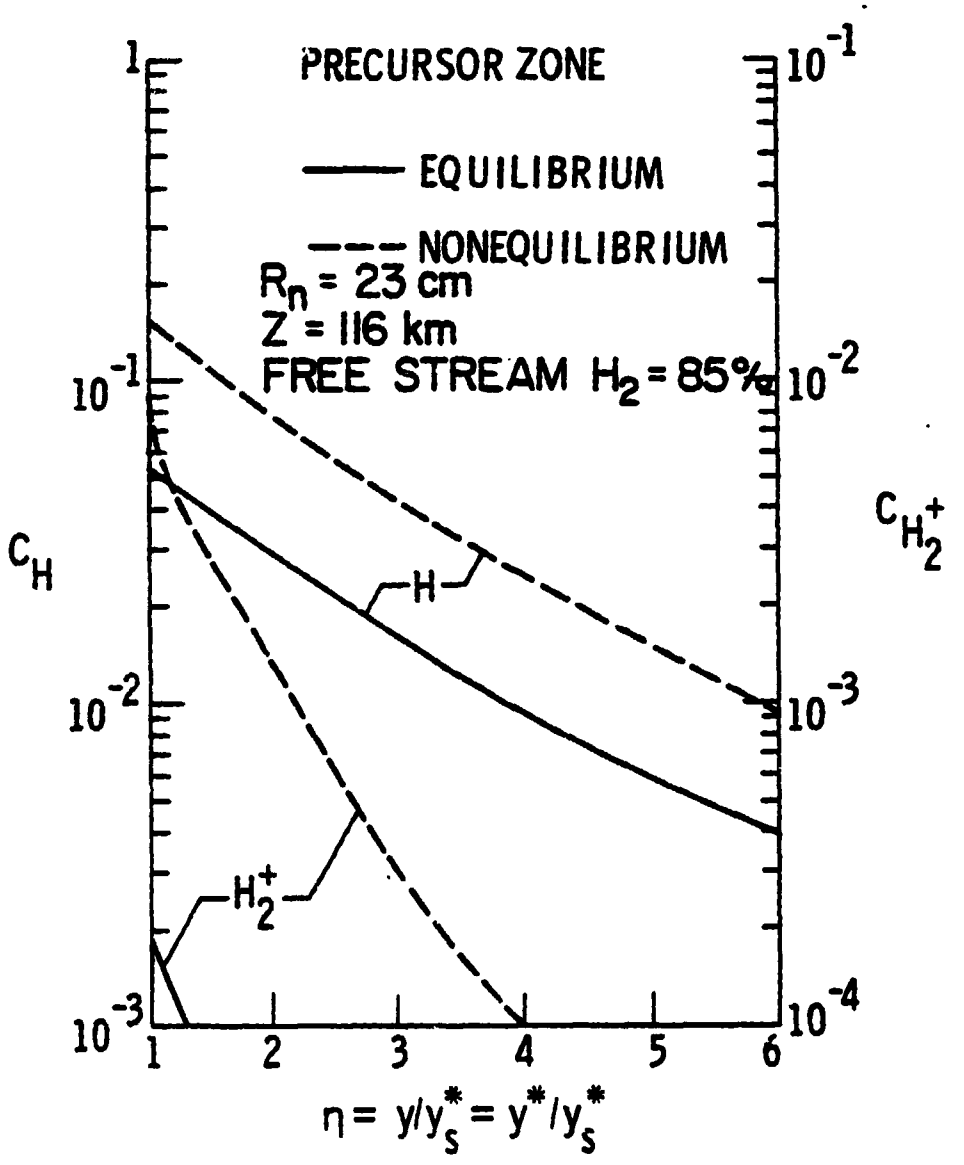

Figure 14. Species concentration in the precursor region for $\xi = 0$.

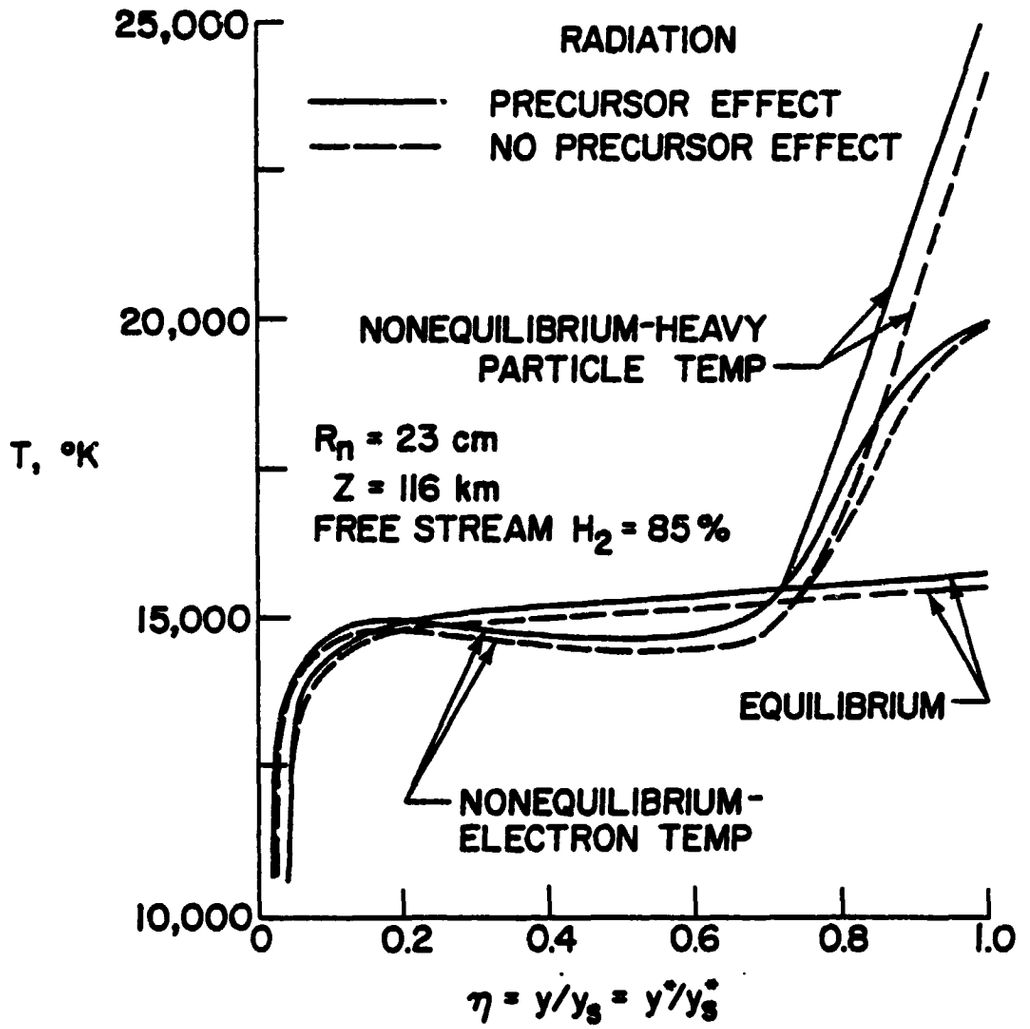

Figure 15. Equilibrium and nonequilibrium temperature variation in the shock layer (with radiation).

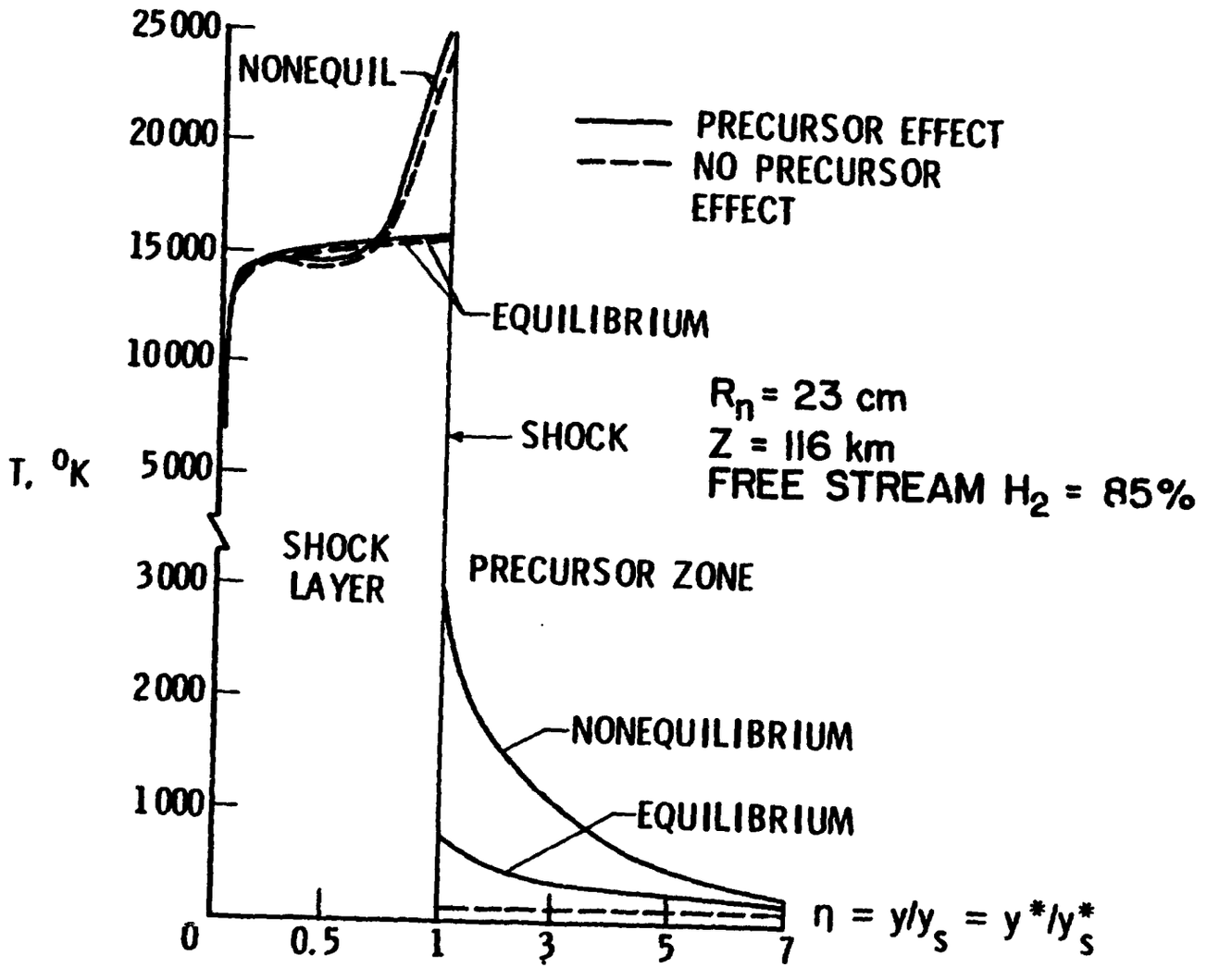

Figure 16. Temperature variation in the shock/precursor region along the stagnation streamline, Z = 116 km.

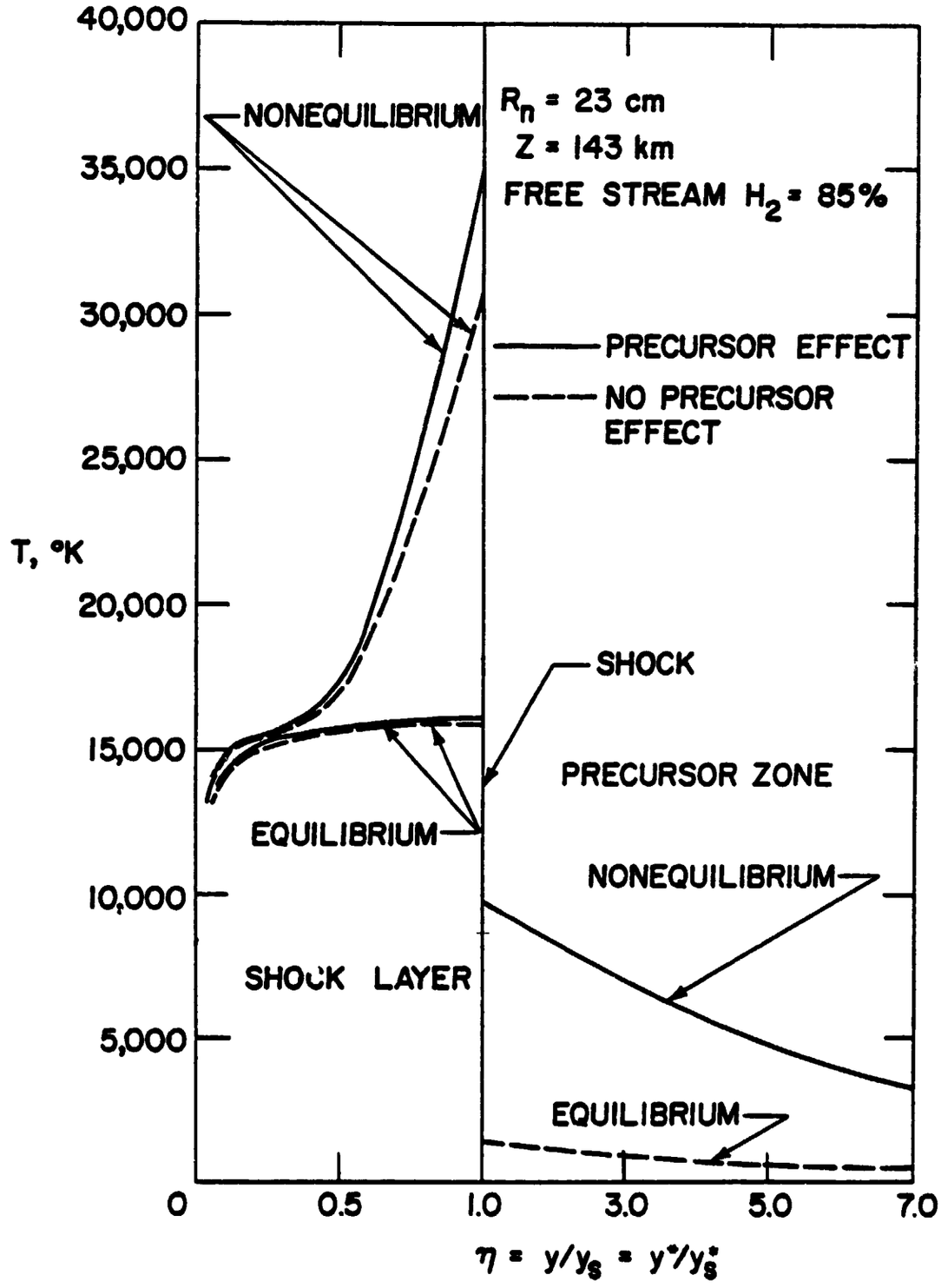

Figure 17. Temperature variation in the shock/precursor region along the stagnation streamline, Z = 143 km.

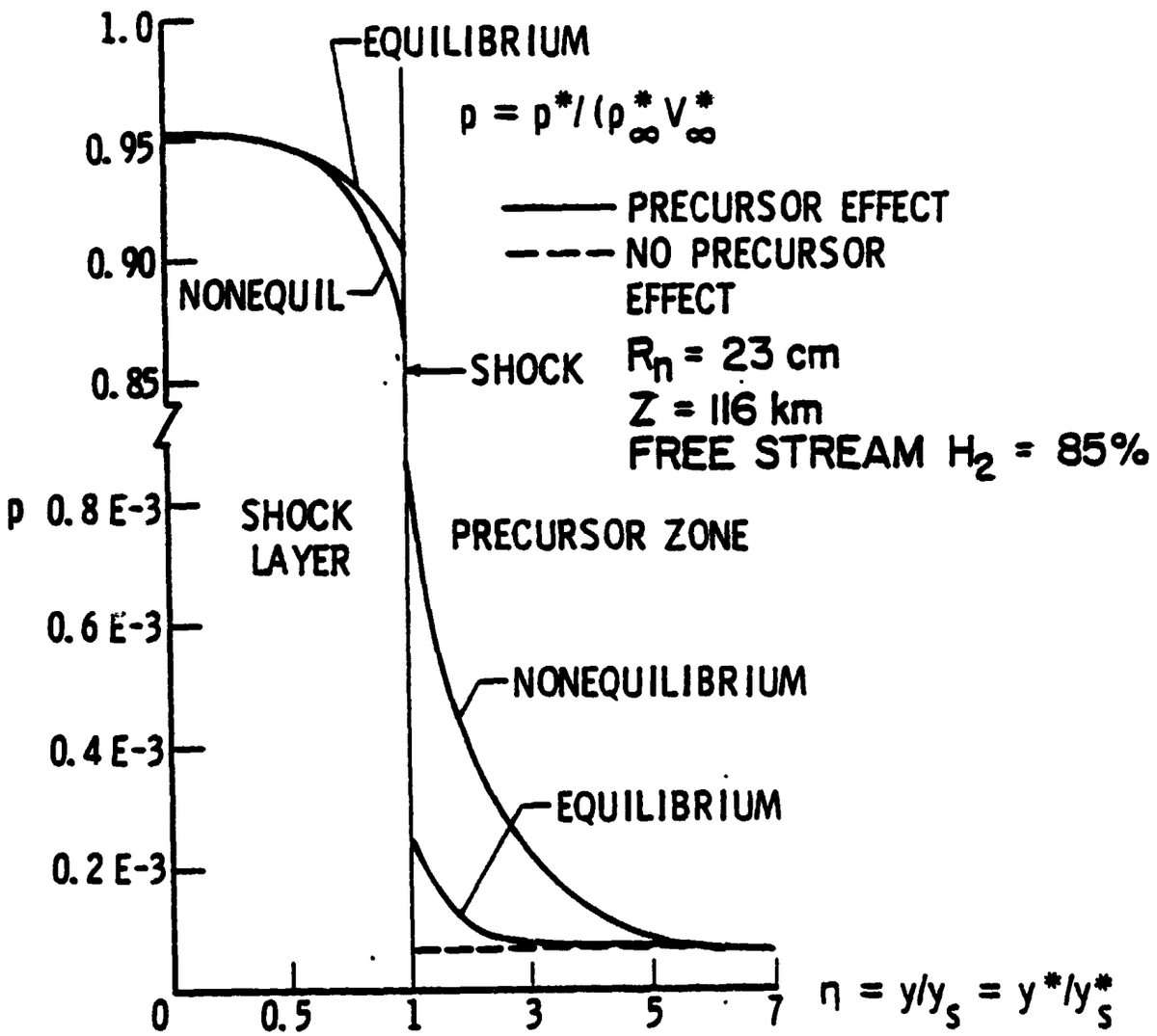

Figure 18. Pressure variation in the shock/precursor region along the stagnation streamline.

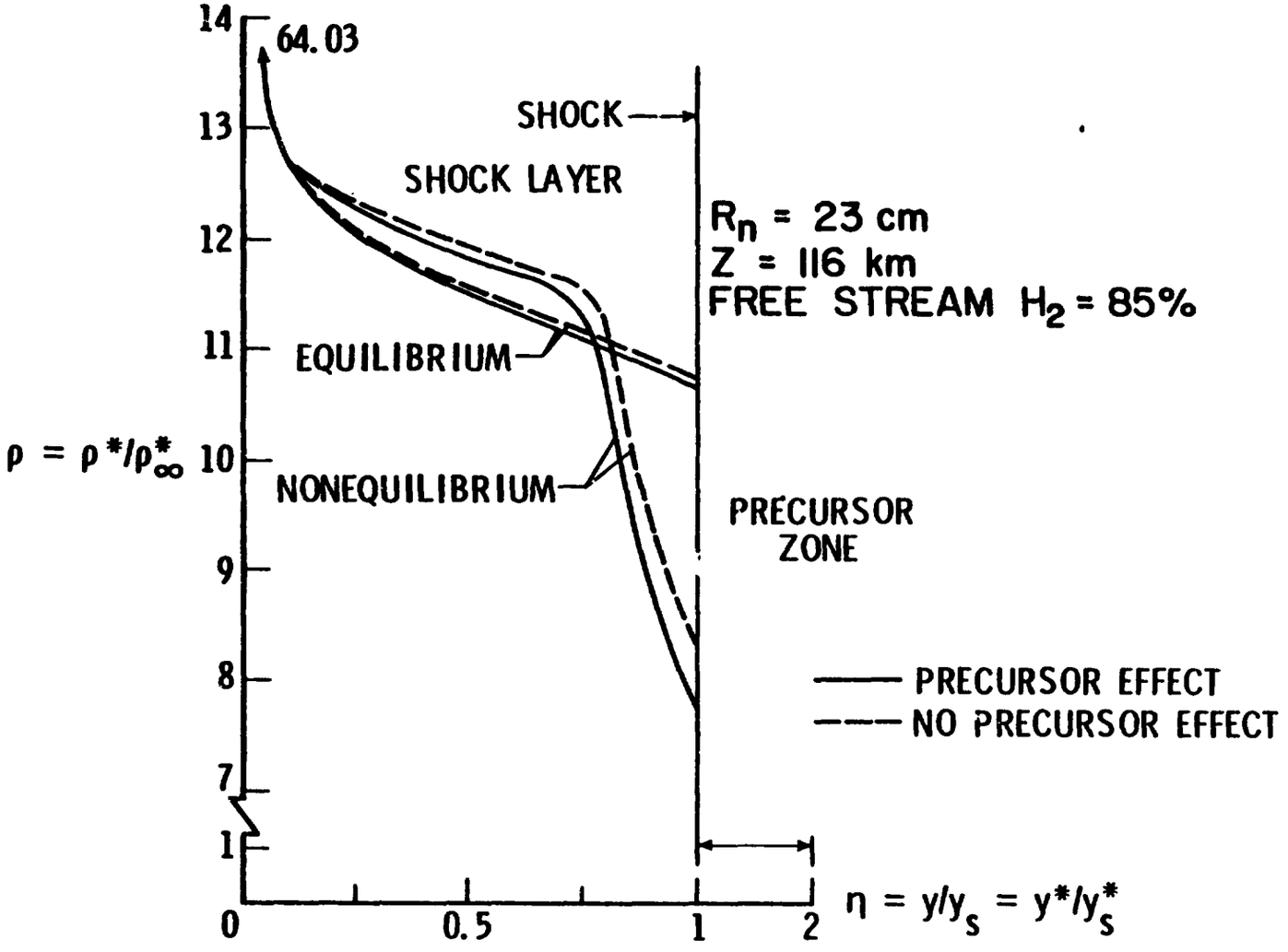

Figure 19. Density variation in the shock/precursor region along the stagnation streamline.

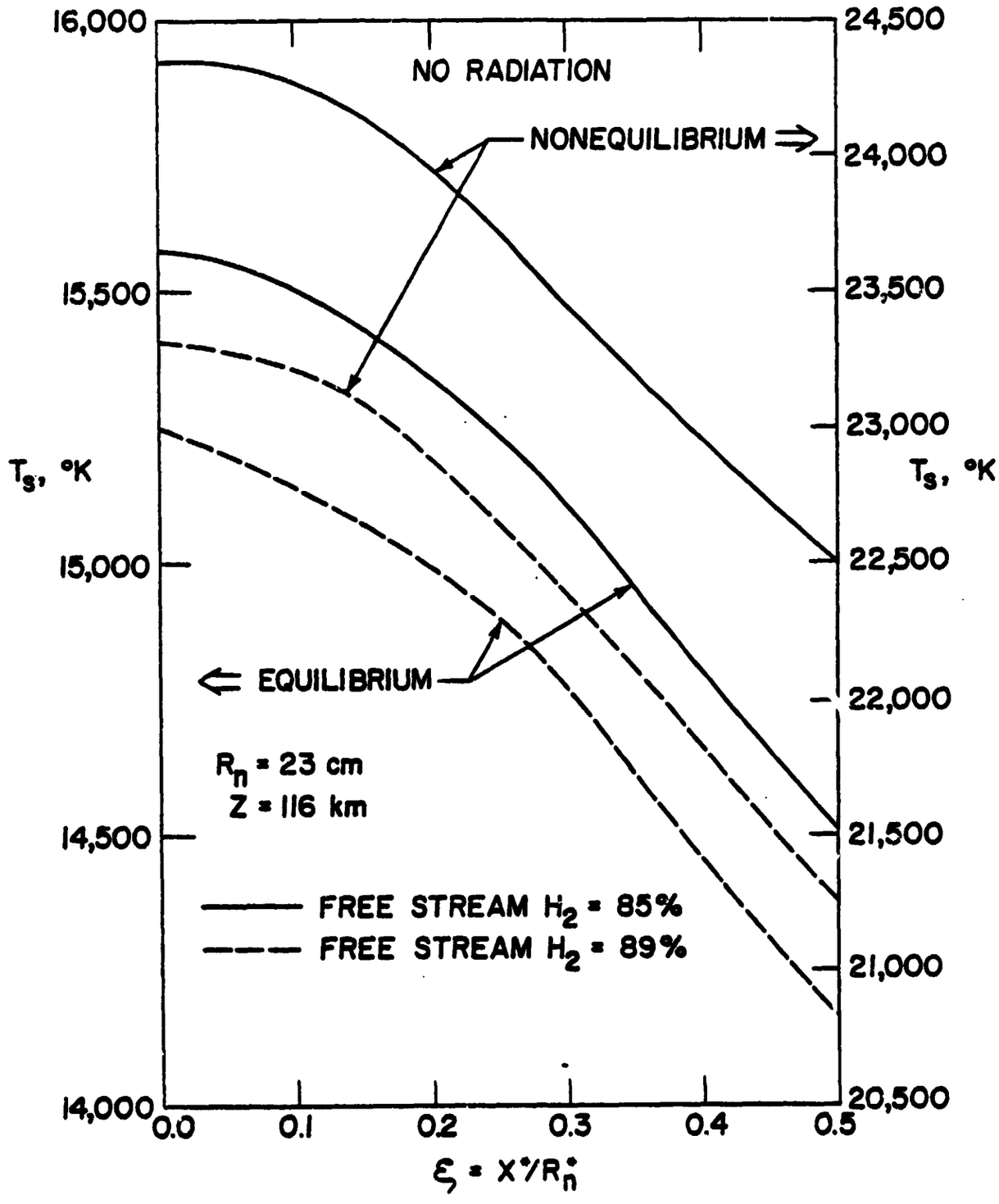

Figure 20. Equilibrium and nonequilibrium shock temperature variation for different free gas stream compositions.

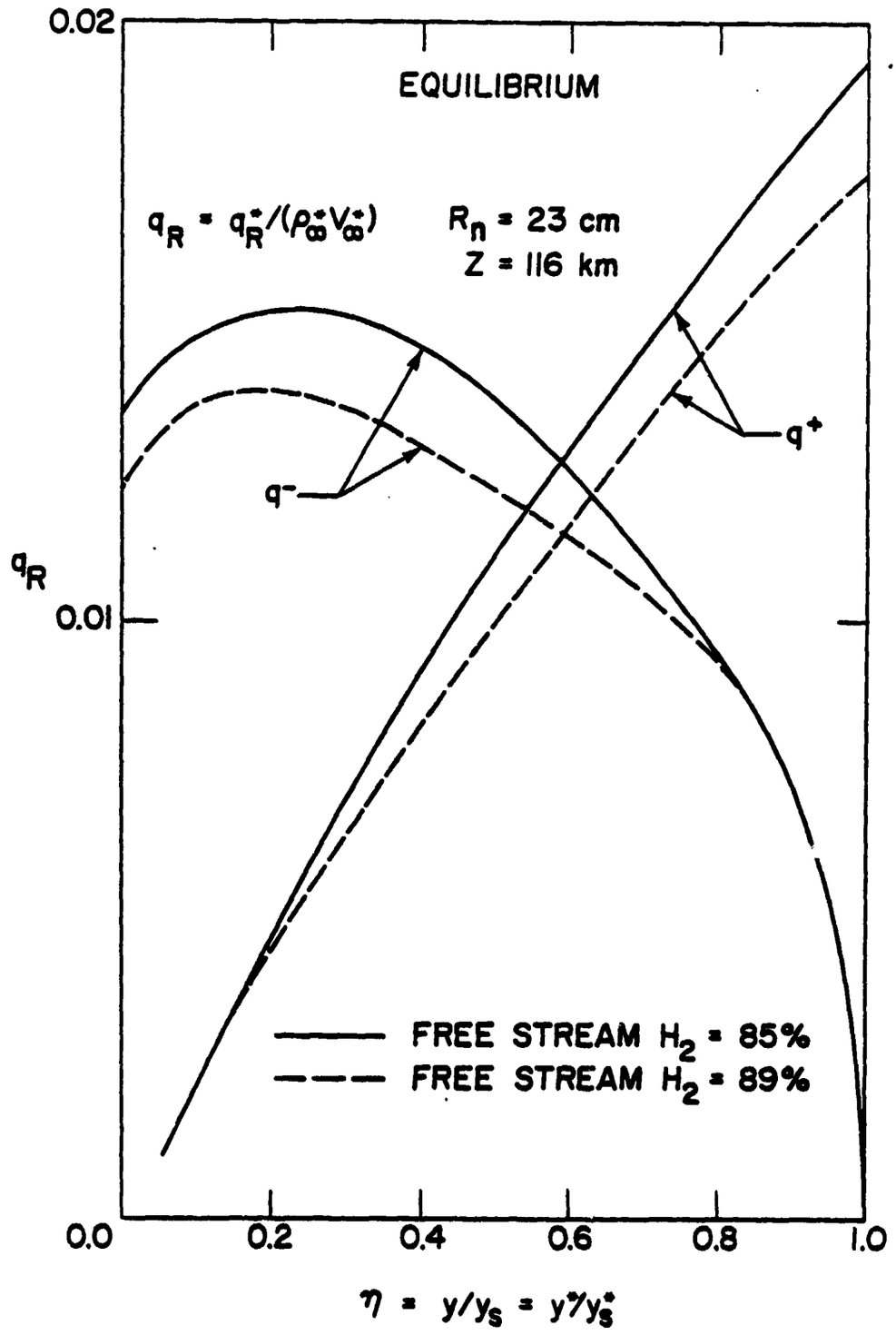

Figure 21. Equilibrium radiative heat flux variation in the shock layer for different free-stream gas compositions.

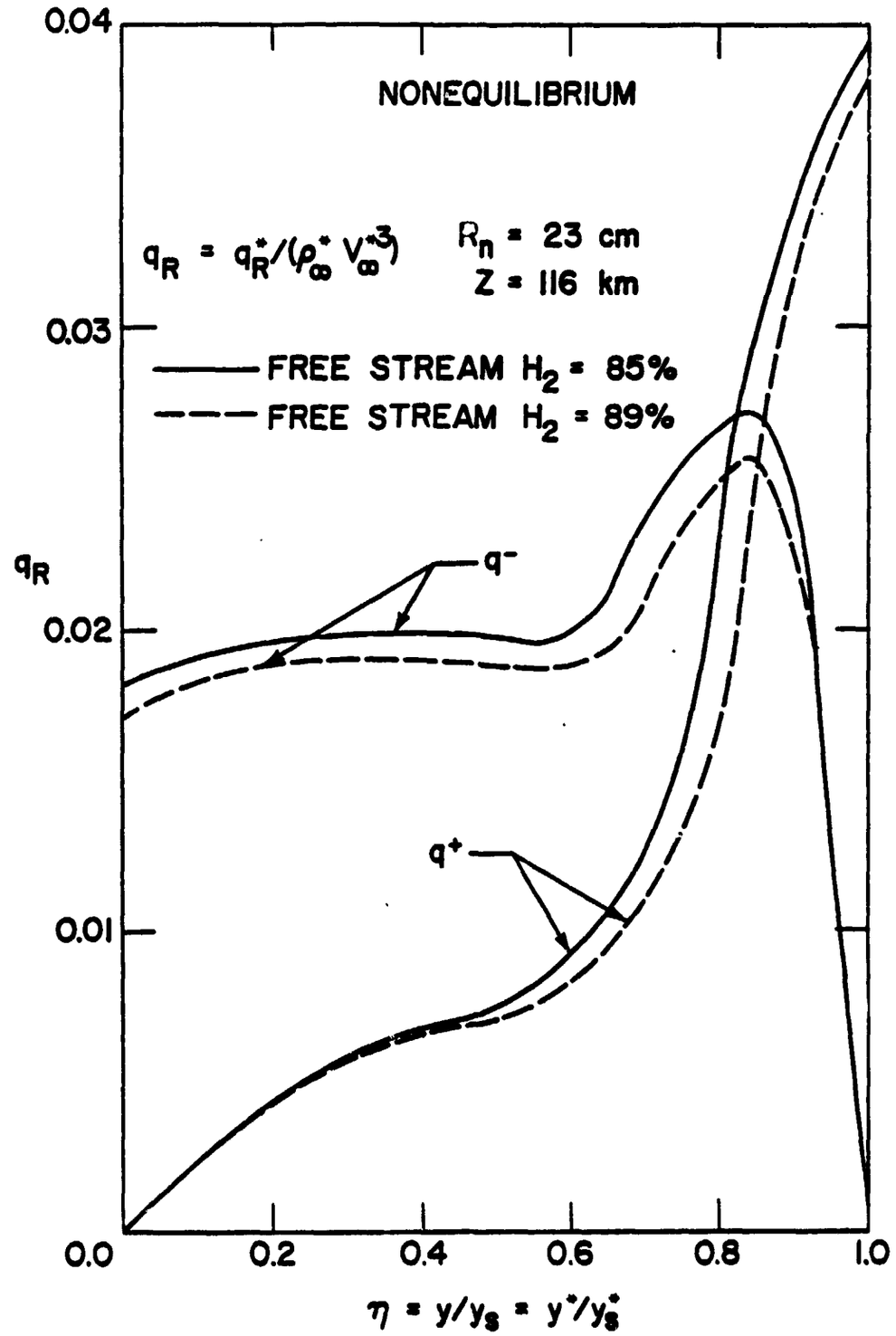

Figure 22. Nonequilibrium radiative heat flux variation in the shock layer for different free-stream gas compos tions.

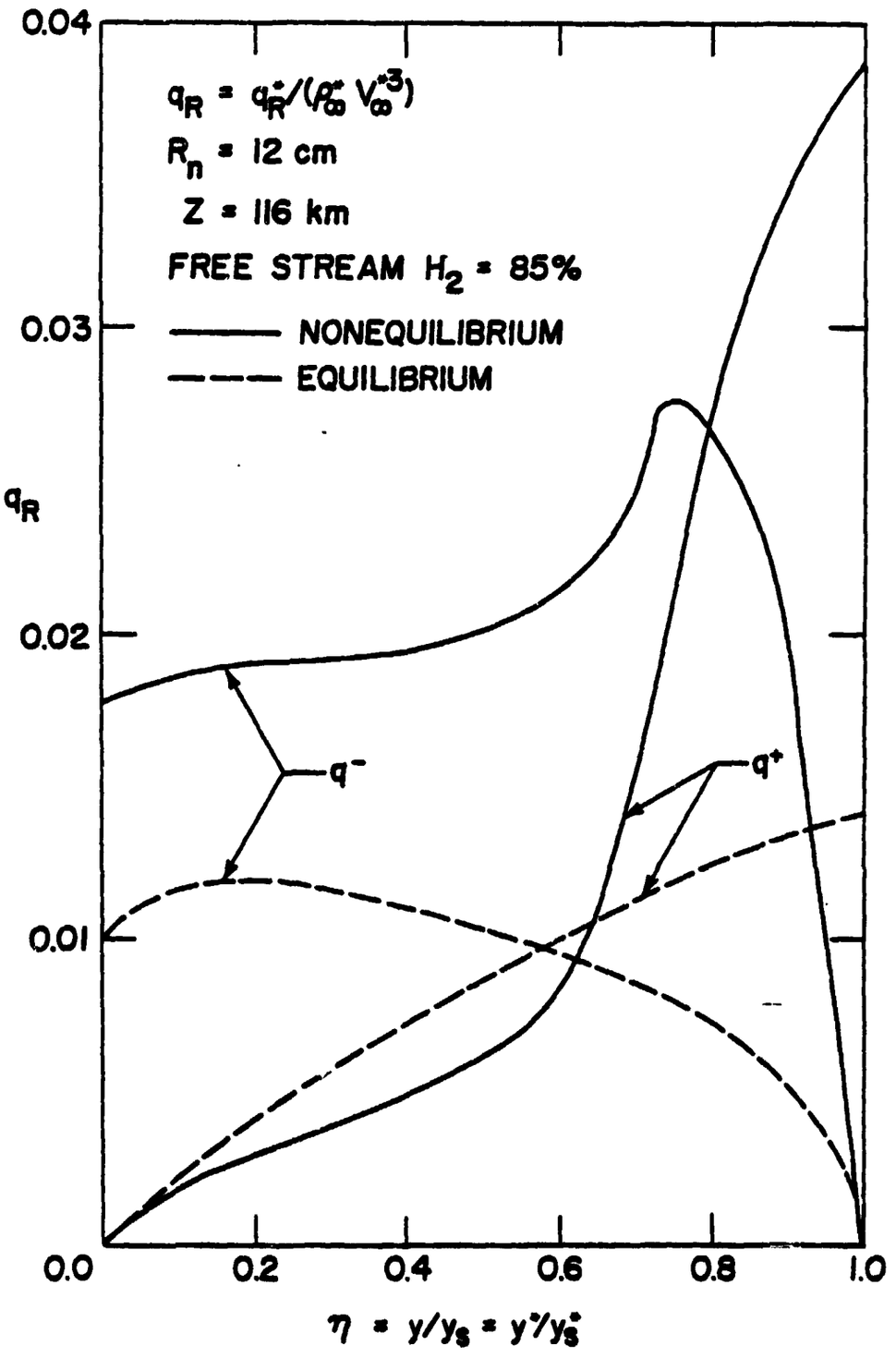

Figure 23. Equilibrium and nonequilibrium radiative heat-flux variation in the shock layer for R_n = 12 cm.

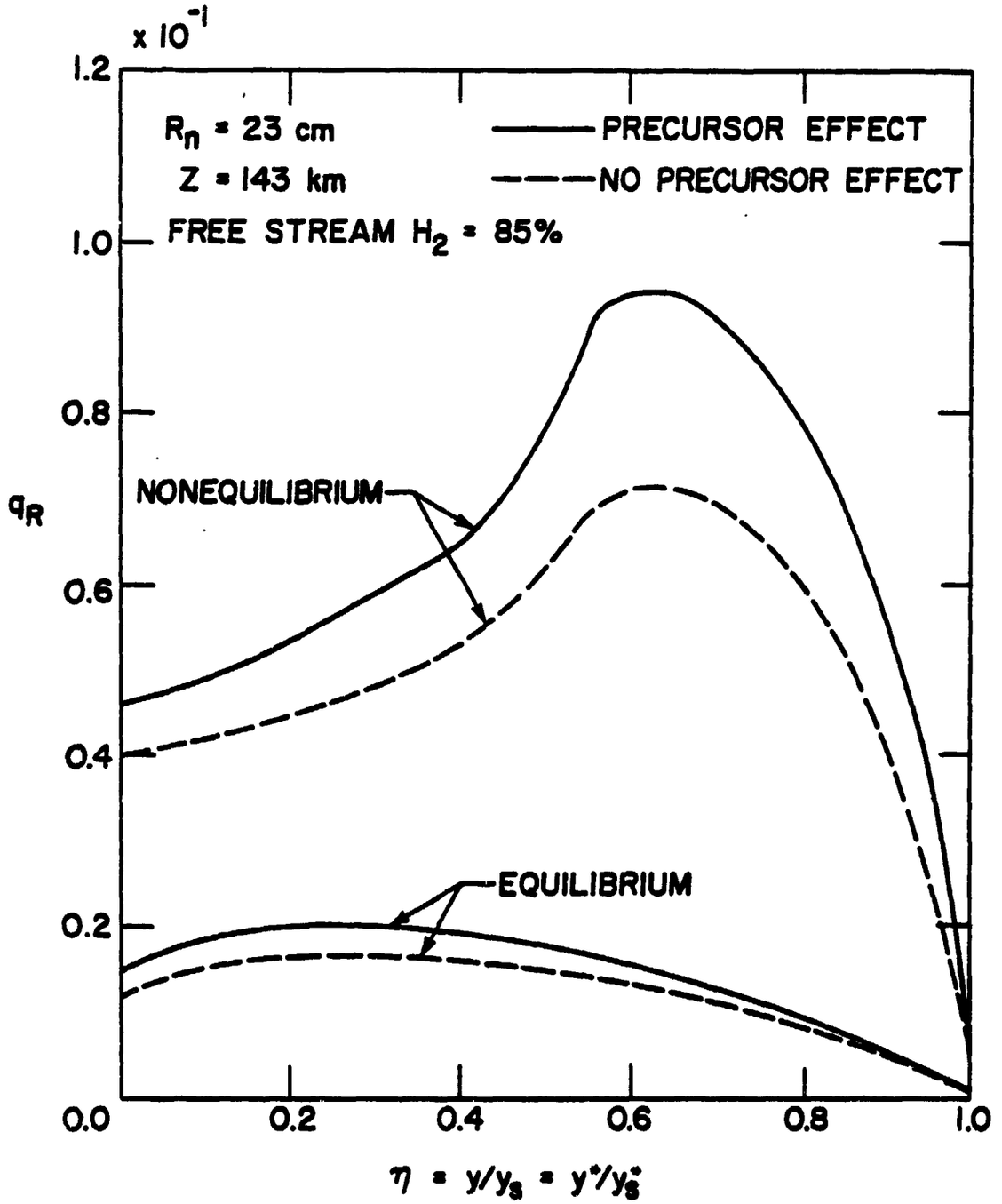

Figure 24. Equilibrium and nonequilibrium radiative heat-flux variation in the shock layer, Z = 143 km.

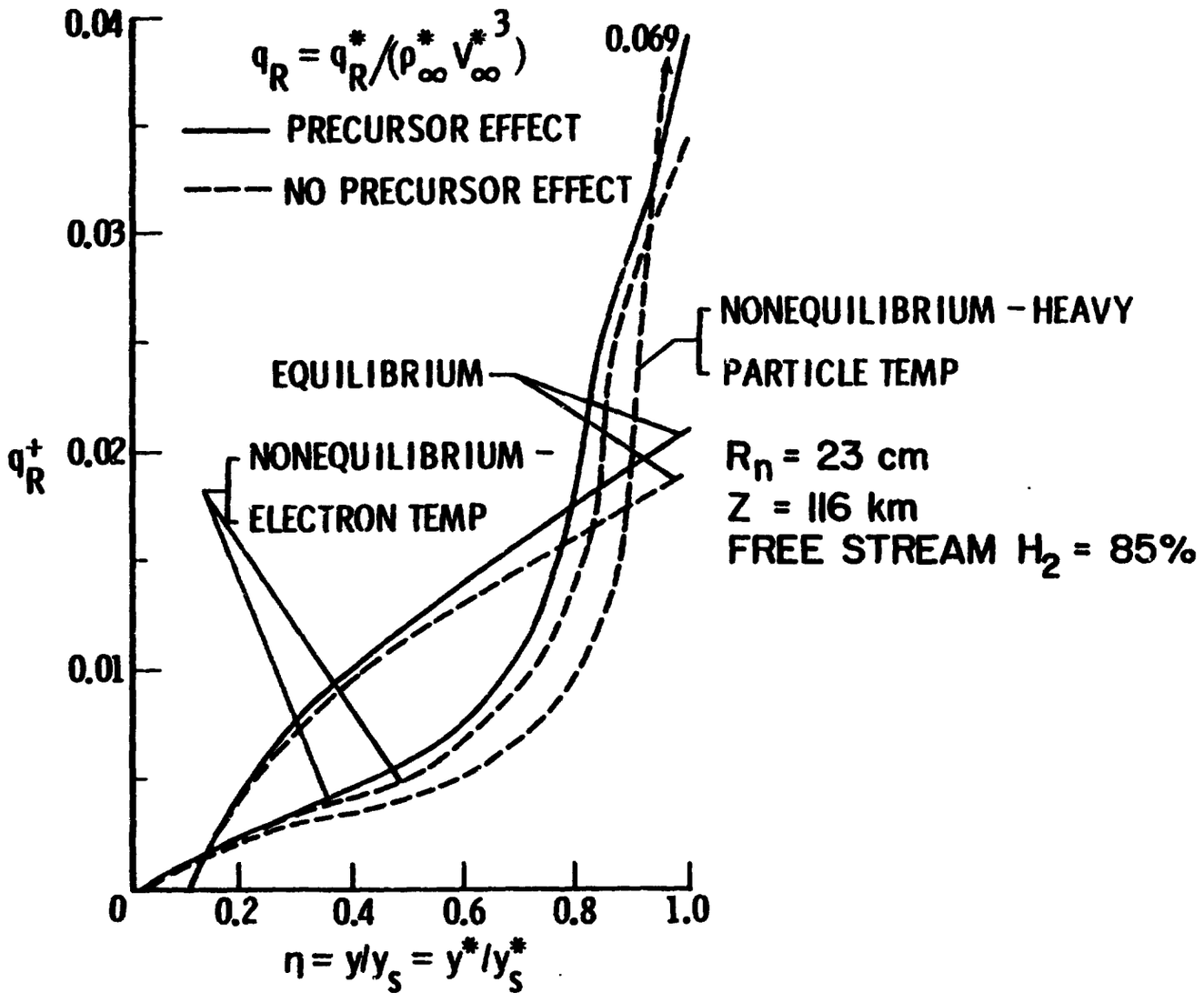

Figure 25. Equilibrium and nonequilibrium radiative heat flux towards the shock for $\xi = 0$.

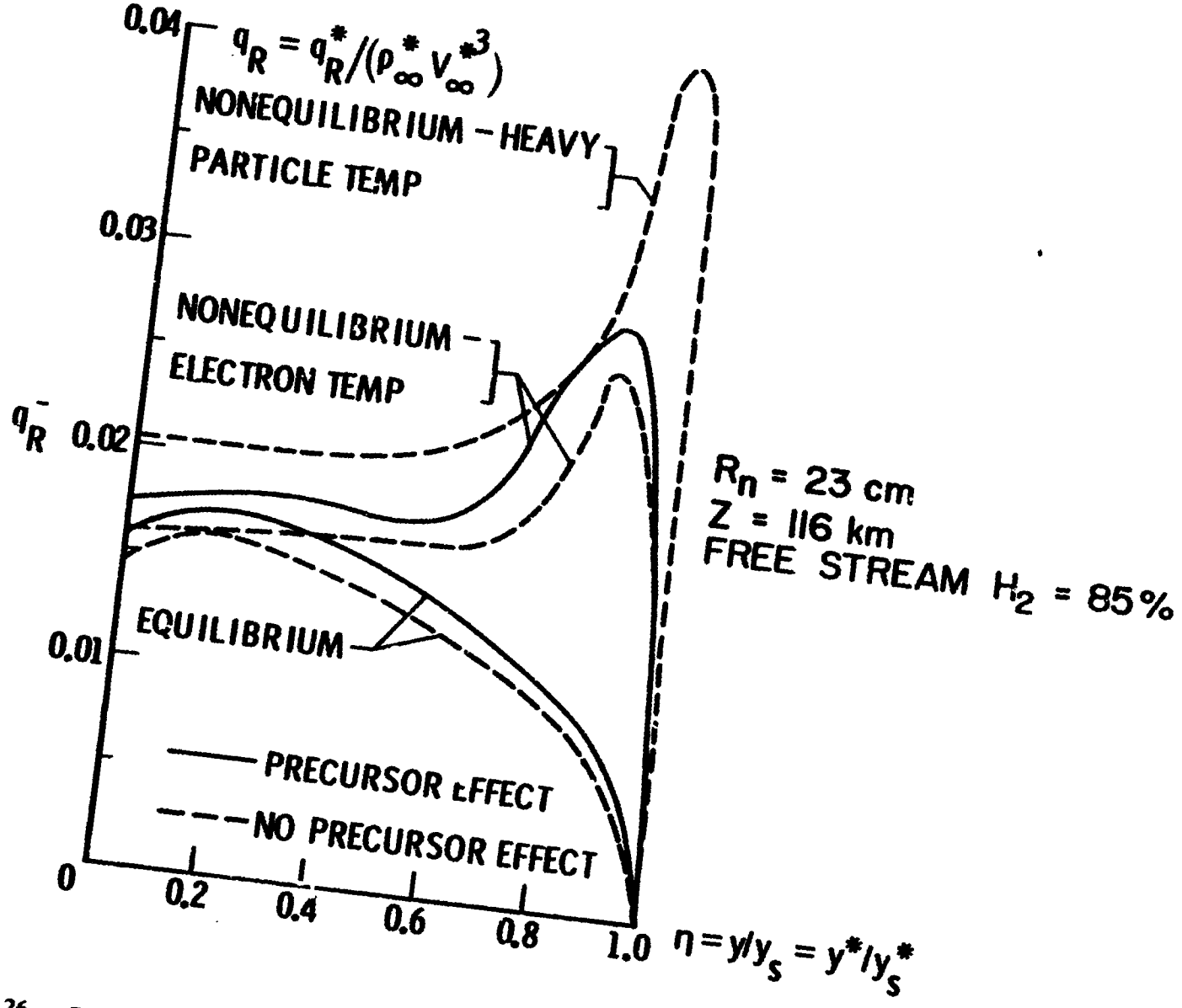

Figure 26. Equilibrium and nonequilibrium radiative heat flux towards the body for $\xi = 0$.

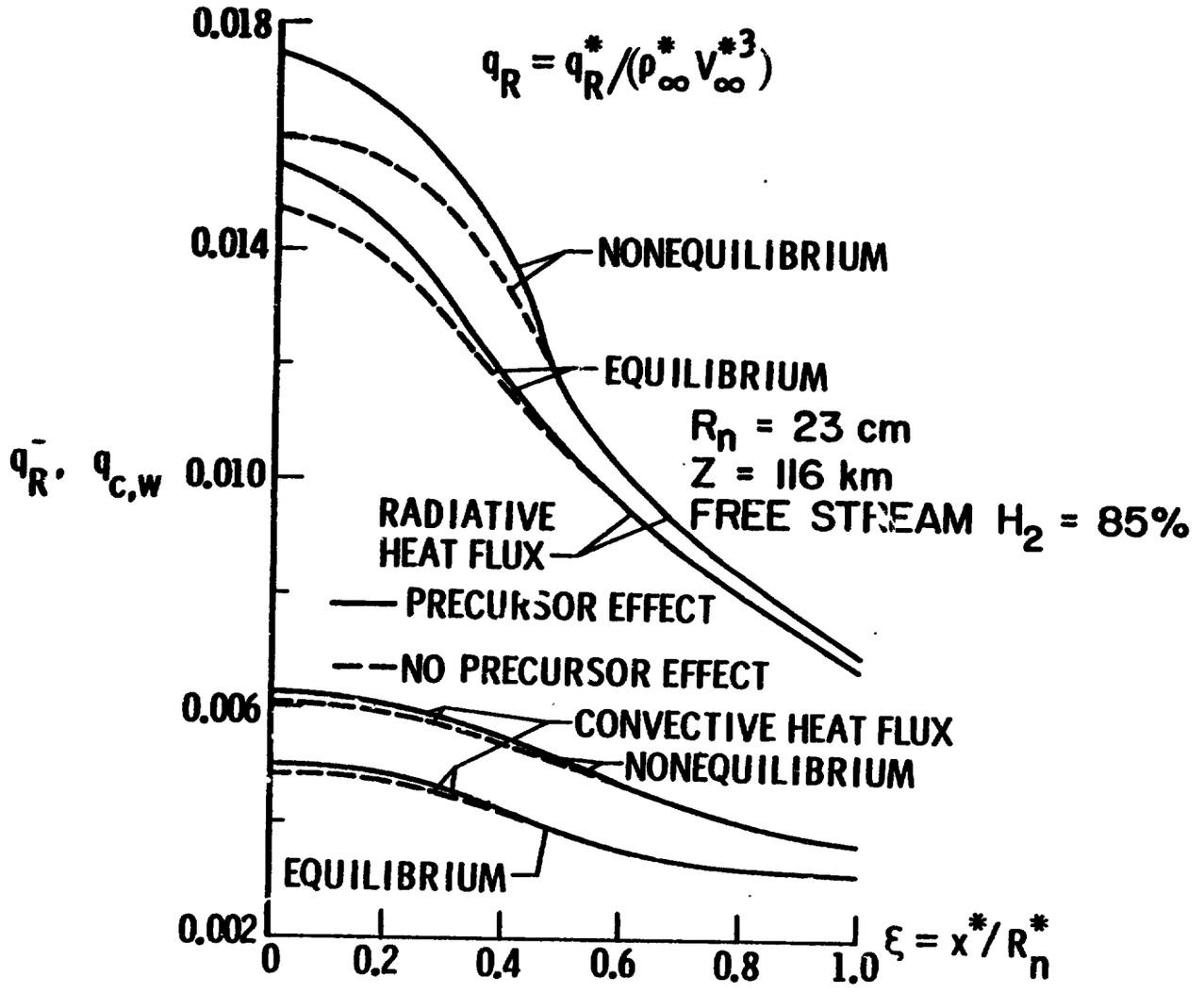

Figure 27. Variation of radiative and convective heat flux with distance along the body surface.